catalysts

MDPI

Review

Research Progress of $ZnIn_2S_4$-Based Catalysts for Photocatalytic Overall Water Splitting

Yujie Yan [1], Zhouze Chen [1], Xiaofang Cheng [1,*] and Weilong Shi [2,*]

[1] School of Environmental and Chemical Engineering, Jiangsu University of Science and Technology, Zhenjiang 212003, China
[2] School of Material Science and Engineering, Jiangsu University of Science and Technology, Zhenjiang 212003, China
* Correspondence: chengxiaofang@just.edu.cn (X.C.); shiwl@just.edu.cn (W.S.)

Abstract: Photocatalytic overall water splitting in solar–chemical energy conversion can effectively mitigate environmental pollution and resource depletion. Stable ternary metal indium zinc sulfide ($ZnIn_2S_4$) is considered one of the ideal materials for photocatalytic overall water splitting due to its unique electronic and optical properties, as well as suitable conduction and valence band positions for suitable photocatalytic overall water splitting, and it has attracted widespread researcher interest. Herein, we first briefly describe the mechanism of photocatalytic overall water splitting, and then introduce the properties of $ZnIn_2S_4$ including crystal structure, energy band structure, as well as the main synthetic methods and morphology. Subsequently, we systematically summarize the research progress of $ZnIn_2S_4$-based photocatalysts to achieve overall water splitting through modification methods such as defect engineering, heterostructure construction, and co-catalyst loading. Finally, we provide insights into the prospects and challenges for the overall water splitting of $ZnIn_2S_4$-based photocatalysts.

Keywords: photocatalytic overall water splitting; $ZnIn_2S_4$; doping; vacancy; heterojunction; co-catalyst

check for updates

Citation: Yan, Y.; Chen, Z.; Cheng, X.; Shi, W. Research Progress of $ZnIn_2S_4$-Based Catalysts for Photocatalytic Overall Water Splitting. *Catalysts* **2023**, *13*, 967. https://doi.org/10.3390/catal13060967

Academic Editor: Jae Sung Lee

Received: 10 May 2023
Revised: 30 May 2023
Accepted: 31 May 2023
Published: 2 June 2023

1. Introduction

The world is currently suffering from environmental pollution and resource depletion, with energy issues looming large. According to relevant studies, the annual global consumption of energy is equivalent to the solar energy reaching the Earth's surface every hour; therefore, solar energy as an abundant, non-polluting natural resource has replaced the traditional fuel fossil as a research hotspot [1]. However, solar energy has limitations such as intermittency and low density, so an effective storage method is needed to make efficient use of solar energy [2]. Since 1972, when it was reported that TiO_2 semiconductors could produce hydrogen and oxygen when irradiated by ultraviolet light, photocatalysis, which uses solar energy to convert it into storable chemical energy, has attracted extensive research [3].

Hydrogen, as a clean, high-energy-density solar fuel, is the ideal energy carrier. Since most photocatalytic hydrogen production studies require the use of sacrificial agents to achieve this, photocatalytic overall water splitting is considered a low-cost, ideal method for converting solar energy into hydrogen energy [4–6]. The photocatalytic overall water splitting process is based on three fundamental photocatalytic processes: photocatalyst absorption of photons to generate electron–hole pairs, photogenerated charge transfer and separation, and surface redox reactions. A variety of semiconductor catalysts such as metal oxides, metal sulfides, and nitrides are currently used in the field of photocatalytic overall water splitting [7–12]. Among them, metal sulfides have the advantages of good charge transfer ability, suitable energy band structure for overall water splitting, and excellent

light collection ability to become one of the potential catalysts in photocatalytic overall water splitting [13].

Metal sulfides are mainly classified into binary metal sulfides such as CdS, MoS_2, and ZnS; ternary metal sulfides such as $ZnIn_2S_4$ and $CuInS_4$; and polymetallic sulfides such as AgZnInS [14]. Most of these binary sulfides have some disadvantages that are more difficult to improve, such as ZnS-based photocatalysts having a poor photo-response, responding only to ultraviolet (UV) light, and CdS-based catalysts having severe photo-corrosion and poor stability, whereas ternary metal sulfides tend to be more stable [15–18]. Zinc indium sulfide ($ZnIn_2S_4$), a ternary metal sulfide belonging to the AB_2X_4 family, has unique electronic and optical properties. Compared with conventional photocatalysts, $ZnIn_2S_4$ has a narrower band gap, adjustable between about 2.06 and 2.85 eV, and has thermodynamically suitable conduction and valence band positions for photocatalytic overall water splitting as well as a strong visible-light response range [19,20]. In addition, $ZnIn_2S_4$ has many advantages such as strong photostability, relatively environmentally friendly chemical composition, ease of preparation, and wide distribution of raw materials [21]. Therefore, $ZnIn_2S_4$ is a more desirable material for photocatalytic overall water splitting.

Although $ZnIn_2S_4$ has many advantages, in practical applications, $ZnIn_2S_4$-based photocatalysts suffer from difficulties in achieving one-component photocatalytic overall water splitting or low photocatalytic overall water splitting efficiency, mainly due to the slow photo-generated charge separation and migration efficiency and weak solar energy utilization [22–24]. Therefore, appropriate modification strategies such as elemental doping, vacancy engineering, the construction of heterojunctions, and the loading of co-catalysts are required to improve the performance of $ZnIn_2S_4$-based photocatalyst materials.

Researchers have actively explored how to improve the performance of $ZnIn_2S_4$-based photocatalysts and have reported on a review of $ZnIn_2S_4$ photocatalysts from different perspectives. For example, Liu et al. reviewed the research progress of $ZnIn_2S_4$-based photocatalysts constructed with heterojunctions for photocatalytic hydrogen production [25]. Yadav et al. reviewed various modification strategies to improve the performance of $ZnIn_2S_4$-based photocatalysts and summarized their applications in water pollution treatment, CO_2 reduction, etc. [26]. However, previous reports are mainly based on applications such as hydrogen production and pollutant treatment, and there is no systematic summary of the research progress on $ZnIn_2S_4$-based photocatalysts for achieving photocatalytic overall water splitting.

Hence, this paper systematically reviews the research progress of $ZnIn_2S_4$-based photocatalysts in photocatalytic overall water splitting. First, we briefly describe the mechanism of photocatalytic overall water splitting. Then, we outline the properties of $ZnIn_2S_4$, including its crystal structure, energy band structure, main synthesis methods, and morphology. The modification strategies of $ZnIn_2S_4$-based photocatalysts are reviewed, mainly including surface engineering such as doping and vacancies, the construction of heterojunctions, and the loading of co-catalysts (Scheme 1). Finally, we provide an outlook on the prospects and challenges of $ZnIn_2S_4$-based photocatalysts for photocatalytic overall water splitting. There are almost no reviews on $ZnIn_2S_4$-based photocatalytic overall water splitting, and the study in this paper provides the latest research progress on $ZnIn_2S_4$-based water splitting catalysts, which is important for the design and synthesis of efficient $ZnIn_2S_4$-based photocatalytic overall water splitting catalysts.

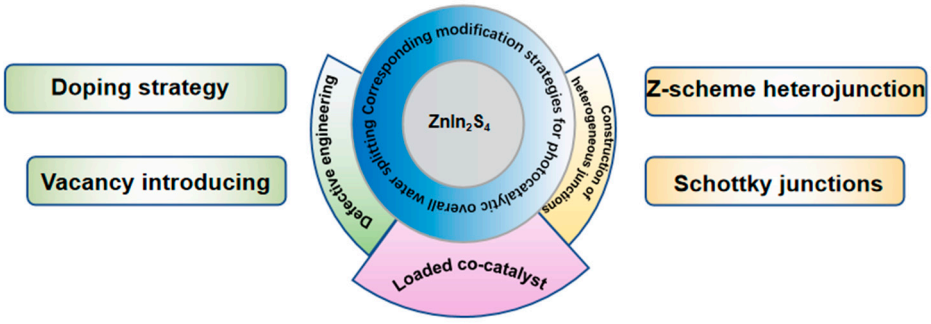

Scheme 1. Modification strategies for $ZnIn_2S_4$-based photocatalysts in photocatalytic overall water splitting are briefly described.

2. Mechanisms of Photocatalytic Overall Water Splitting

Photocatalytic overall water splitting consists of two half-reactions, the hydrogen evolution reaction (HER) and the oxygen evolution reaction (OER). Theoretically, in order to achieve overall water splitting, the semiconductor band gap should be no less than 1.23 eV under standard conditions, the potential at the bottom of the conduction band should be less than 0 eV (H_2/H^+ = 0 eV vs. NHE, pH = 0), and that at the top of the valence band should be greater than 1.23 eV (H_2O/O_2 = 1.23 eV vs. NHE, pH = 0) [27]. The redox potential of water is all located within the band gap of the photocatalyst and photocatalytic overall water splitting is thermodynamically feasible. However, photocatalytic overall water splitting is an uphill reaction requiring additional energy to promote water splitting, which is a thermodynamically unfavorable process (G > 0); therefore, hydrogen and oxygen are prone to the reverse reaction and H_2O reformation, which severely inhibits the photocatalytic water splitting activity [28].

Semiconductor-based photocatalysts for photocatalytic overall water splitting are based on three basic processes of photocatalysis: under solar irradiation with an energy greater than the band gap of the photocatalyst, photogenerated electrons are excited to leap to the conduction band and photogenerated holes remain in the valence band; photogenerated charges migrate separately to the semiconductor reaction site; and un-recombined photogenerated electrons and holes undergo redox reactions of water at the catalyst surface [29]. From the kinetic point of view, the recombination of photogenerated carriers is much faster than their redox reactions at the surface. The Coulomb force constraints between photogenerated charges and high interfacial potential barriers during charge transfer lead to rapid photogenerated carrier recombination and low utilization efficiency, which severely limit photocatalytic activity [30].

In addition, the range of solar energy utilization affects the photocatalytic activity. According to relevant research reports, the UV content of natural sunlight is less than 3%, the visible content is less than 40%, and the near-infrared occupies about 50% of the sunlight, while photocatalytic materials capture light basically in the UV and visible region, with a low efficiency of solar energy utilization [31,32]. The overall photocatalytic water splitting activity is limited by the low light collection capacity of the catalyst, the rate of photogenerated charge separation and migration, and the surface oxidation reaction [33]. Therefore, researchers have adopted corresponding modification strategies to prepare photocatalysts with high activity and high solar energy utilization efficiency. The stable ternary metal sulfide $ZnIn_2S_4$ is one of the ideal materials for photocatalytic overall water splitting due to its advantages. As shown in Scheme 2, the $ZnIn_2S_4$-based photocatalysts have thermodynamically suitable conduction and valence band positions for photocatalytic water splitting. However, single-component photocatalytic water splitting is difficult to achieve due to the overall low charge utilization and solar utilization as well as photocorrosion phenomena. Therefore, modification strategies such as the doping of heteroatoms, formation of defects, construction of heterojunctions, and loading of co-catalysis were adopted to enhance the $ZnIn_2S_4$-based photocatalytic performance.

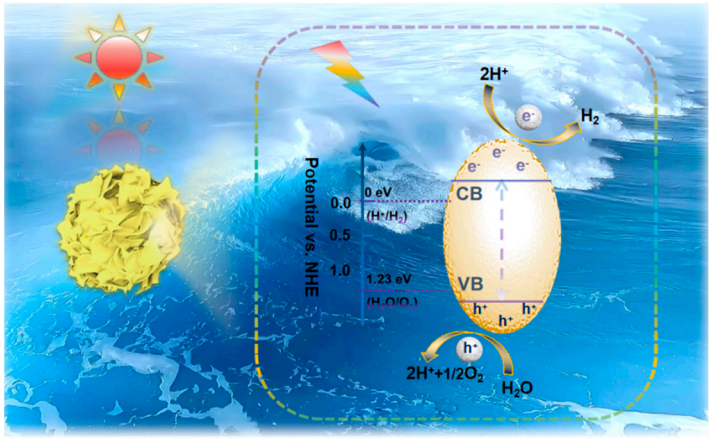

Scheme 2. Schematic diagram of $ZnIn_2S_4$-based photocatalyst photocatalytic overall water splitting.

3. Introduction of $ZnIn_2S_4$

3.1. Crystal and Energy Band Structures

The ternary metal sulfide $ZnIn_2S_4$ has three crystal phase structures: cubic, hexagonal, and rhombic. As shown in Figure 1a, the cubic $ZnIn_2S_4$ has an ABC stack in which the Zn atom is tetrahedrally coordinated to the S atom and the In atom is octahedrally coordinated to the S atom [34]. As shown in Figure 1b, the hexagonal $ZnIn_2S_4$ has a layered structure in which the atoms are repeatedly stacked in the order S-Zn-S-In-S-In-S. In the hexagonal crystal phase, the Zn atoms and half of the In atoms form a tetrahedral coordination with the S atoms, and the remaining In atoms form an octahedral coordination with the S atoms [35]. As shown in Figure 1c, the crystal structure of rhombic $ZnIn_2S_4$ is similar to that of hexagonal $ZnIn_2S_4$, consisting of a sandwich layer with one octahedron and two tetrahedra. Rhombic $ZnIn_2S_4$ differs from hexagonal $ZnIn_2S_4$ in that the Zn atoms and half of the In atoms are mixed in the tetrahedral sites [36]. Different crystalline phases have different properties, the cubic phase has thermoelectric properties, the hexagonal phase has photoconductivity, and the rhombic phase has good charge transfer ability. In addition, the researchers found that the photocatalytic activity of $ZnIn_2S_4$ can be effectively enhanced by changing the crystalline phase. For example, in 2011, Shen et al. synthesized $ZnIn_2S_4$ with different crystalline phase structures by high-temperature thermal sulfide treatment of metal oxide precursors [37]. They performed thermal sulfidation reactions on Zn-In mixed oxide precursors under an H_2S atmosphere and synthesized cubic $ZnIn_2S_4$ and gradually transformed it into rhombohedra when the thermal sulfidation temperature was increased from 400 to 800 °C. The rhombohedral $ZnIn_2S_4$ has a good charge transfer ability and light absorption, enhancing the photocatalytic hydrogen production activity under sacrificial agents. In addition, $ZnIn_2S_4$ can be used to transform the crystalline phase by using different metal precursors and changing the reaction temperature to prepare more active crystalline phases and structures for photocatalytic applications. Density functional theory (DFT) has been widely used in semiconductor materials to study the electronic structure of materials. DFT provides theoretical insight into the electronic energy band structure of cubic, hexagonal, and rhombic $ZnIn_2S_4$, and all three crystalline phases are direct band gap semiconductors. Although the respective band gaps of the cubic, hexagonal, and rhombic crystalline phases are known from theoretical calculations, the actual band gaps deviate from the calculated results due to the limitations of the local density approximation (LDA) functional [38].

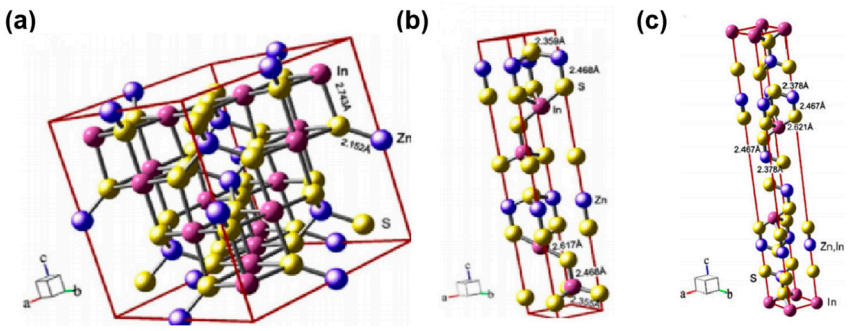

Figure 1. Crystal structure of cubic (**a**), hexagonal (**b**), rhombic (**c**) $ZnIn_2S_4$ [37].

3.2. Synthetic Methods and Morphology of $ZnIn_2S_4$

3.2.1. Morphology of $ZnIn_2S_4$

The conformation and structure of $ZnIn_2S_4$, a stable ternary metal sulfide semiconductor, significantly affect the photocatalytic activity. Among them, $ZnIn_2S_4$ with different morphological structures such as zero-dimensional (0D), one-dimensional (1D), two-dimensional (2D), and three-dimensional (3D) plays an important role in the solar–chemical energy conversion process.

Zero-dimensional $ZnIn_2S_4$ is mainly available in quantum dots (QD). Quantum dots, as a hot research material in the energy environment, have the advantages of easy synthesis, abundant surface sites, and controllable size, and due to the quantum confinement effect, their light collection range can be adjusted to the near-infrared region, which significantly improves the solar light utilization effect [39]. Peng et al. prepared size-tunable $ZnIn_2S_4$ quantum dots using oleylamine as the ligand and uncoordinated octadecene as the solvent [40]. Due to the different effects of reaction temperature in controlling the nucleation and growth process of nanocrystals thermodynamically and kinetically, $ZnIn_2S_4$ nanocrystals with sizes ranging from 2.1 to 10.1 nm were synthesized by varying the reaction temperature between 140 °C and 210 °C. Experiments have shown that $ZnIn_2S_4$ nanocrystals with small size and annealed to remove the capping agent are highly active in the degradation of methylene orange. Currently, 1D $ZnIn_2S_4$ is mainly available as nanowires, nanotubes, and nanoribbons, but most 1D $ZnIn_2S_4$ synthesis requires the use of templates, so most of the synthesized morphologies are 2D and 3D $ZnIn_2S_4$ [41,42]. The majority of $ZnIn_2S_4$ syntheses are hexagonal due to the advantages of good stability, simple preparation, and high activity of the hexagonal crystalline phase $ZnIn_2S_4$. It is easy for the hexagonal $ZnIn_2S_4$ layered structure to form a 2D nanosheet morphology; especially, the ultra-thin 2D nanosheets have the advantages of short photogenerated carrier migration distance, large specific surface area, and abundant surface-active sites, which significantly improve the photocatalytic activity of $ZnIn_2S_4$-based materials [43]. In 2018, Zhang et al. prepared ultrathin $ZnIn_2S_4$ nanosheets (Vs-M-$ZnIn_2S_4$) rich in S-vacancies by exfoliating large blocks of $ZnIn_2S_4$ synthesized using lithium intercalation [44]. Then, MoS_2 quantum dots (MoS_2QDs) were grown in the S-vacancy region of Vs-M-$ZnIn_2S_4$ induced by S-vacancies in one of the Zn cuts to synthesize atomic-level heterojunction MoS_2QDs@Vs-M-$ZnIn_2S_4$. Unlike $ZnIn_2S_4$, the S-vacancies in MoS_2QDs@Vs-M-$ZnIn_2S_4$ act as electron traps, enriching electrons in the Zn plane and transferring them to MoS_2QDs via Zn-S bonds, preventing the rapid recombination of photogenerated charges due to vertical electron transport and improving the hydrogen production activity of the photocatalyst.

However, due to the high surface energy of the individual nanosheets, $ZnIn_2S_4$ tends to aggregate to form 3D microspheres during growth, and both the specific configuration of its synthesis and the increased specific surface area and active sites enhance the photocatalytic activity of the catalyst. Shen et al. synthesized persimmon-layered $ZnIn_2S_4$ photocatalysts by using an oleylamine (OA)-assisted solvent method, adding tetrahydrofuran (THF) solution to form a hexagonal structure and OA selectively adsorbed on the $ZnIn_2S_4$ hexagon to form nanoplates, which then self-assembled to form persimmon [45]. The material has

excellent photocatalytic hydrogen production activity, with the best catalyst achieving 220.45 mmol h^{-1} after 3% Pt loading. Some of the $ZnIn_2S_4$ photocatalysts synthesized in current research, such as marigold and peony-flower-like, as well as rose and marigold-like, are 3D microspheres [46,47]. Furthermore, hollow structured materials with their rich surface-active sites, short charge migration paths, and good light collection capabilities have attracted the interest of a wide range of researchers [48]. In 2014, Warule et al. synthesized hollow marigold-like $ZnIn_2S_4$ materials for photocatalytic hydrogen production by a surfactant-assisted hydrothermal method [49]. The hollow marigold-like nanoparticles have a higher specific surface area and more active sites, exhibiting better hydrogen production activity. As most photocatalytic reactions occur on the surface of the material, the morphology and configuration of the material have an important influence on the photocatalytic activity. The synthesis of materials with high specific surfaces, abundant active sites, and unique configurations is very important for improving the performance of $ZnIn_2S_4$. We provide a brief summary of the various morphologies of $ZnIn_2S_4$ in Table 1.

Table 1. Summary of different morphologies and synthesis methods for hexagonal phase $ZnIn_2S_4$ photocatalysts.

Type	Morphology	Photocatalyst	Synthetic Method	Sulfur Source	Solvent	Light Source	Application	Ref
0D	quantum dots	$ZnIn_2S_4$	solvothermal	sulfur powder	octadecene	500 W Xe lamp	degradation	[40]
1D	nanowires	$ZnIn_2S_4$	wet-chemical	thioacetamide (TAA)	H_2O	500 W Xe lamp	degradation	[41]
1D	nanotubes	$ZnIn_2S_4$	wet-chemical	TAA	H_2O	500 W Xe lamp	degradation	[41]
2D	ultrathin nanosheet	Vs-M-$ZnIn_2S_4$	lithium intercalation	TAA	N,N-Dimethylformamide, ethylene glycol	300 W Xe lamp	hydrogen generation	[44]
3D	persimmon-like shape	$ZnIn_2S_4$	solvothermal	CS_2	tetrahydrofuran (THF)	300 W Xe lamp	hydrogen generation	[45]
3D	porous $ZnIn_2S_4$ submicrospheres	$ZnIn_2S_4$	microwave-solvothermal	excess thiourea	ethylene glycol	300 W tungsten–halogen	degradation	[46]
3D	peony-flower-like	$ZnIn_2S_4$	solventhermal	dioctyldithiocarbamic acid sodium (OTC)	CH_3OH	300 W tungsten-halogen	degradation	[47]
3D	rose-flower-like microsphere	$ZnIn_2S_4$	hydrothermal	thiourea	H_2O, diethyl amine (DEA)	300 W Xe lamp	hydrogen generation	[49]
3D	hollow marigold-like flowers	$ZnIn_2S_4$	hydrothermal	thiourea	H_2O, polyvinyl pyrrolidone (PVP)	300 W Xe lamp	hydrogen generation	[49]
3D	porous microspheres	$ZnIn_2S_4$	microwave-sol vothermal	excessive TAA	H_2O	500 W tungsten–halogen lamp	degradation	[50]
3D	hollow Structure	$ZnIn_2S_4$	hydrothermal	glutathione (GSH)	H_2O	300 W Xe lamp	hydrogen generation	[51]

3.2.2. Synthetic Methods of $ZnIn_2S_4$

Hydrothermal method. Unlike other synthesis methods that use templates and special equipment, the hydrothermal synthesis of $ZnIn_2S_4$ is relatively gentle and simple. The reaction temperature, the type of reaction precursor, the pH of the reaction system, the use of surfactants, and the type of surfactant all influence the synthesis, morphology, and crystallinity of the $ZnIn_2S_4$-based catalysts. In 2006, Guo et al. prepared $ZnIn_2S_4$ solid and hollow microsphere structures hydrothermally under cetyltrimethylammonium bromide (CTAB) and ethylene glycol (PEG) as surfactants, respectively [52]. Two different $ZnIn_2S_4$ crystalline phase materials were hydrothermally synthesized by the addition of different metal precursors by Chen et al. in 2012 [53]. The cubic phase was synthesized when metal nitrates were added as precursors, whereas a thermodynamically stable hexagonal phase was prepared when metal chlorides containing electronegative low-chloride ions were used as precursors. In addition, Warule et al. in 2014 synthesized hollow marigold-like and rose-shaped $ZnIn_2S_4$ photocatalysts by a surfactant-assisted hydrothermal method using polyvinylpyrrolidone (PVP) and diethylamine (DEA), respectively [49]. Studies have shown that varying the concentration of PVP (100 ppm–300 ppm) results in the synthesis

of different forms ranging from twisted to hollow marigold-like. In 2022, Yin et al. synthesized $ZnIn_2S_4$ with different assembled microstructures for dehydrogenation treatment by a one-step hydrothermal method and investigated the effect of different solvents on the structure of $ZnIn_2S_4$ [54]. The experimental results showed that the solvents were water, ethanol, and ethylene glycol in accordance with which smooth surface-petal-like, relatively rough micro-disk-like and thin nanosheets were synthesized. In 2022, Zou et al. hydrothermally prepared $ZnIn_2S_4$ materials with different crystalline phases by adjusting the pH of the system using oxalic acid as a chelating agent [55]. The cubic phase of $ZnIn_2S_4$ was prepared without the addition of oxalic acid and hydrothermal preparation after oxalic acid modification transformed the original cubic phase of $ZnIn_2S_4$ into a hexagonal phase.

Solvothermal method. Like hydrothermal methods, solvothermal synthesis is relatively simple and is widely used in the synthesis of materials for the energy environment. The nature of the solvent such as alkalinity, viscosity, and type of solvent play an important role in the preparation of $ZnIn_2S_4$ materials in terms of their morphology. Guo et al. in 2006 found that reaction temperature has a significant effect on $ZnIn_2S_4$ morphology [52]. They prepared the catalysts by varying the reaction temperature solvothermally using pyridine as the solvent; when the reaction temperature was between 120 and 160 °C, $ZnIn_2S_4$ grew in the (002) direction to form nanoribbons, and when the reaction temperature was 180 °C and higher, the material formed nanotubular shapes. In addition to the reaction temperature, the type of solvent has an equally important influence on the synthetic microstructure of $ZnIn_2S_4$. In 2008, Shen et al. used water, methanol, and ethylene glycol as solvents, with the first two synthesizing cherry-shaped microspheres and ethylene glycol as the solvent to synthesize micro-clustered clusters [56]. The results show that the catalysts synthesized with water as the solvent are more crystalline and stable and have the best hydrogen production efficiency. Furthermore, Su et al. in 2016 used water, ethanol, methanol, as well as ethylene glycol as solvent precursors for the synthesis of $ZnIn_2S_4$ by a solvothermal method to investigate the effect of different types of solvents on the selective oxidation activity of aromatic alcohols [57]. The experimental structures showed that the best photocatalytic performance of $ZnIn_2S_4$ was prepared using ethanol as the solvent, and that the difference in performance between the different solvents was mainly due to the degree of exposure of the basic crystalline surface, resulting in different exposures of the special surface.

Other synthesis methods. In addition to hydrothermal and solvothermal methods, microwave-assisted methods, thermal sulfur methods, chemical vapor deposition, and spray pyrolysis are also applied to the synthesis of $ZnIn_2S_4$ in different forms and structures [58–60]. In 2012, Huang et al. synthesized $ZnIn_2S_4$ in micro-spherical form by a simple spray pyrolysis method [61]. They first synthesized the solution by magnetic stirring, then atomized the solution and fed it into a tubular reactor for reaction to produce spherical particles. In addition, Pop et al. in 2022 prepared $ZnIn_2S_4$ photocatalysts by the microwave-assisted oil bath production method to investigate the effect of $ZnIn_2S_4$ materials with different zinc concentrations and reaction temperatures on methyl orange adsorption [62]. The experimental results show that disordered cubic $ZnIn_2S_4$ is synthesized at 160 °C and hexagonal phase $ZnIn_2S_4$ structures are synthesized at 180 °C. Moreover, the morphology changes from nanoparticles to nanoflower, hollow-microsphere structures as the zinc concentration and reaction temperature increase. Although there are numerous methods to synthesize $ZnIn_2S_4$, hydrothermal and solvothermal methods are widely used in the synthesis of $ZnIn_2S_4$-based photocatalysts due to the advantages of the simple synthesis process and low cost.

Since most catalytic reactions occur on the surface of catalysts, the structure and morphology of materials have important effects on their properties. Therefore, we briefly describe representative morphologies in $ZnIn_2S_4$ materials as well as hydrothermal and solvothermal synthesis methods. It is hoped that this will provide some reference for the preparation of $ZnIn_2S_4$ photocatalytic overall water splitting morphologies using simple synthetic methods.

4. Photocatalytic Overall Water Splitting Modification Based on $ZnIn_2S_4$ Catalyst

4.1. Defect Engineering

Defect engineering not only modulates the electronic structure, provides abundant active sites, and improves the efficiency of charge separation and migration of materials, but also changes the morphology and interfacial reactions of materials and plays an important role in the catalytic reactions of materials [63]. Therefore, defect engineering is often used in photocatalytic systems to modulate material properties, among which metal sulfides have received a lot of attention because of their tunable electronic structure. Doping and vacancies, which are point defects in defect engineering, have been applied to modulate material properties in sulfide catalysts such as $ZnIn_2S_4$. Su et al. synthesized Al^{3+}-doped strontium calcium titanate photocatalysts (Al-STO) for photocatalytic overall water splitting by polymerization complexation [64]. The doping of low-valence metal cations effectively promotes the migration rate of photogenerated carriers, and the appropriate oxygen vacancies on the surface facilitate the adsorption of water molecules and hydroxyl groups to promote the reduction reaction. The reduction in intrinsic Ti^{3+} defects effectively promotes the separation and migration efficiency of photogenerated carriers in concert with the oxygen vacancies on the surface to improve the photocatalytic activity of strontium-titanate-based photocatalysts. The best material—2% Al-STO—achieved hydrogen yields of 1.256 mmol h^{-1} and oxygen yields of 0.692 mmol h^{-1} under a loaded co-catalyst, with an apparent quantum efficiency (AQE) of up to 55.46% at 365 nm for the composite. It follows that the introduction of defects in semiconductor photocatalysts is a promising method of modification.

4.1.1. Doping Strategy

Doping strategies are modification methods that introduce impurity atoms, such as metals and non-metals, into the structure of photocatalytic materials to form defects to alter the material properties, mainly through both doping and ion exchange [65,66]. Material doping with heteroatoms has the advantages of narrowing the band gap of the composite, enhancing light absorption, changing the morphological structure of the material, and increasing the separation and migration rates of photogenerated carriers, and is therefore considered to be an effective method for effectively increasing the activity of sulfide photocatalysts [67]. Alkaline earth metals such as Ca and Ba, rare-earth metals such as La and Y, transition metals such as Ag, Co, and Ni, as well as non-metals such as N and O have been employed in $ZnIn_2S_4$, and good photocatalytic activity has been achieved [68].

Metal Doping

Pan et al. in 2021 reported Ag-$ZnIn_2S_4$ composite photocatalytic materials with dual defects in Ag doping and nanopores prepared by cation exchange between 2D $ZnIn_2S_4$ monolayers and Ag, achieving $ZnIn_2S_4$ photocatalytic overall water splitting without co-catalysts and sacrificial agents under visible light irradiation [69]. The experimental results show that Ag doping can effectively narrow the band gap, improve the light collection capacity of the catalyst, and promote photogenerated charge separation. The hydrogen yield of the composites was 56.6 μmol g^{-1} h^{-1} and the oxygen yield was 29.1 μmol g^{-1} h^{-1}. The Ag-$ZnIn_2S_4$ composite has good photocatalytic activity, as shown in Figure 2a; the Ag element doping redistributes the charge; the positively charged enriched Ag adsorbs water molecules and promotes the oxygen production reaction; and the sulfur atoms suspended on the nanopores promote the hydrogen production reaction. In addition, the ultrathin 2D $ZnIn_2S_4$ monolayer narrows the migration distance and increases the photogenerated charge separation and migration rate. They also prepared Cu-$ZnIn_2S_4$ with a similar structure to Ag-$ZnIn_2S_4$ by the same method. The experimental results show that Cu doping has a stronger charge migration rate and higher hydrogen production activity, but as shown in Figure 2b, Cu doping does not enable photocatalytic all-water decomposition, which confirms that Ag doping is important for the Ag-$ZnIn_2S_4$ materials to achieve photocatalytic all-water decomposition.

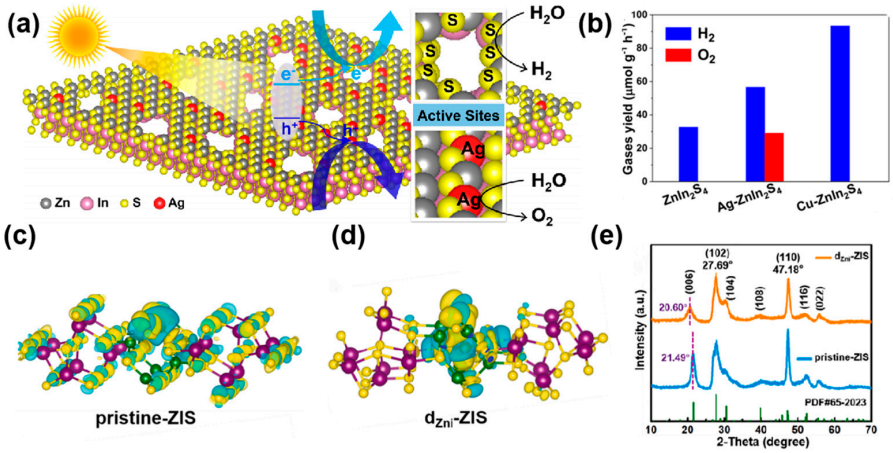

Figure 2. (**a**) Schematic illustration of the dual-defect (Ag dopants and nanoholes) configuration established on $ZnIn_2S_4$ monolayers and (**b**) comparison of the H_2 and O_2 evolution activities of $ZnIn_2S_4$, Ag-$ZnIn_2S_4$, and Cu-$ZnIn_2S_4$ in photocatalytic water-splitting reaction under visible-light illumination (300 W xenon lamp, λ > 420 nm) [69]. The differential charge density maps for pristine-ZIS atomic layers (**c**) and dZni-ZIS atomic layers (**d**), and (**e**) X-ray diffraction (XRD) patterns of pristine-ZIS and dZni-ZIS [70].

In addition, in 2022, Sun et al. used a magnetic stirring one-step solvothermal method to synthesize in situ interstitial zinc-doped ultrathin $ZnIn_2S_4$ nanosheets (dZni-$ZnIn_2S_4$) and to study the photocatalytic performance of the materials for photocatalytic overall water splitting without any auxiliary agent under visible-light irradiation [70]. The Zn doping not only produces a static potential difference, but also forms a short range of disordered structures with abundant active sites. As shown in Figure 2e, the Zn doping leads to broadening and weakening of the $ZnIn_2S_4$ (006) peak and disruption of interlayer stacking, and widens the material nanosheet spacing, forming a short-range disordered structure. The differential charge density map (Figure 2c,d) reveals that, unlike the original $ZnIn_2S_4$ with uniform charge density distribution, dZni-$ZnIn_2S_4$ leads to charge redistribution with positive charge enrichment at the Zn site, lowering the water oxidation potential barrier and increasing the electron density at the sulfur site, which facilitates H^+ adsorption reduction and improves the photocatalytic overall water splitting activity. In addition, the ultrathin nanosheets formed by the dZni-$ZnIn_2S_4$ material shorten the migration distance and effectively promote photogenerated carrier separation, achieving a hydrogen yield of 42.8 μmol g^{-1} h^{-1} and an oxygen yield of 19.1 μmol g^{-1} h^{-1}.

Subsequently, Sun et al. in 2022 also used a magnetic stirring one-step solvothermal method to synthesize Al-$ZnIn_2S_4$ composites and investigate their hydrogen and oxygen production properties under visible-light irradiation [71]. Al-$ZnIn_2S_4$ has a rich mesoporous structure that maximizes the exposure of active sites and enhances photocatalytic activity. The Al doping also produces an expanded layer spacing that induces a domain electrostatic potential difference, effectively promoting photogenerated carrier separation. Al doping redistributes the charge, enriching the Al sites with positive charge, increasing the electron density around the S sites, promoting redox reactions in the material, reducing photocorrosion, and improving stability. Due to these characteristics, the material achieves efficient photocatalytic overall water splitting without any auxiliary agent, with a hydrogen yield of 77.2 μmol g^{-1} h^{-1} and an oxygen yield of 35.3 μmol g^{-1} h^{-1}.

Non-Metal Doping

Jing et al. prepared $ZnIn_2S_4$-350 °C-4 h with oxygen doping and S-vacancies by hydrothermal synthesis of hexagonal $ZnIn_2S_4$ by calcination at 350 °C under an air atmosphere for 4 h [72]. The calcined $ZnIn_2S_4$ improves light absorption, and the surface-rich S-vacancies extend the photogenerated charge lifetime to inhibit recombination but do not increase the carrier density. The increase in electron paramagnetic resonance (EPR) signal

after calcination indicates that calcination introduces S-vacancies, which increases and then decreases with increasing calcination time, and that the surface oxygen doping gradually fills in. After air calcination, the Fourier-transform infrared (FTIR) spectrum shows SO_4^{2-} bidentate characteristic peaks, further demonstrating the synergistic effect of the material between the oxygen doping and the S-vacancies. The synergistic effect of S-vacancies and oxygen doping on the material surface enhances photogenerated carrier lifetimes and concentrations and improves the photocatalytic overall water splitting activity. The materials are loaded with Pt/Cr co-catalyst and show remarkable photocatalytic activity with a hydrogen yield of 270.2 μmol g^{-1} h^{-1} and an oxygen yield of 130.0 μmol g^{-1} h^{-1}, which are 13 times higher than those of the pristine $ZnIn_2S_4$.

In summary, compared with the undoped $ZnIn_2S_4$-based material, the material doping element can effectively reduce the band gap of the composite material, improve the material's light collection capacity, change the morphological structure of the material, modulate the electronic structure of the material, and increase the photogenerated carrier separation and migration rate. Although the role of doping elements in photocatalysis remains in doubt due to their possible negative effects as photogenerated charge recombination centers, doping strategies do play an important role in modifying $ZnIn_2S_4$-based photocatalytic materials.

4.1.2. Vacancy Introduction

Vacancies are material lattice defects caused by the lack of cations or anions, which is mainly divided into cationic and anionic types [73]. He et al. prepared single-atom sulfur vacancy CdS nanorods (Sv-CdS NRs) with a spin-polarized electric field by the hydrothermal method combined with anaerobic heating to achieve photocatalytic overall water splitting without any co-catalyst [74]. Single-atom sulfur vacancies are introduced to induce spin-polarization properties in the CdS system, providing a strong facilitating electric field that enhances photogenerated carrier separation and migration rates. Sv-CdS NRs significantly improves the photocatalytic activity of the material, and the best material, Sv-CdS-2 NRs, was able to achieve a hydrogen evolution performance of 363.8 μmol g^{-1} h^{-1} and an oxygen evolution performance of 181.9 μmol g^{-1} h^{-1}. In 2022, a rhombic $ZnIn_2S_4$-800 material rich in S-vacancies was reported by Jing et al. [75]. They designed and prepared a rhombic crystal phase and sulfur-vacancy-rich $ZnIn_2S_4$-800 material by calcining hexagonal $ZnIn_2S_4$ at high temperature under a nitrogen atmosphere, unlike the previous harsh preparation conditions, which changed the crystal phase of $ZnIn_2S_4$. As shown in Figure 3a, X-ray diffraction (XRD) patterns of $ZnIn_2S_4$ before and after calcination show that high-temperature calcination under a nitrogen atmosphere has modified the crystal phase and structural morphology of $ZnIn_2S_4$. Characterization by electron paramagnetic resonance (Figure 3b), UV-diffuse reflectance spectroscopy (Figure 3c), and the energy band structure (Figure 3d) confirms that the introduction of sulfur vacancies into $ZnIn_2S_4$ by calcination has narrowed the band gap and improved the light gathering capacity of the material. Appropriate S-vacancies as electron capture sites to increase the photogenerated carrier density inhibit recombination and promote hydrogen production reactions, and the calcined material has a smaller average mass of electrons and holes, accelerating the rate of photogenerated charge migration. The material loaded with Pt/Cr co-catalyst achieves hydrogen yields of 68.0 μmol g^{-1} h^{-1} and oxygen yields of 31.0 μmol g^{-1} h^{-1} in pure water under visible-light irradiation.

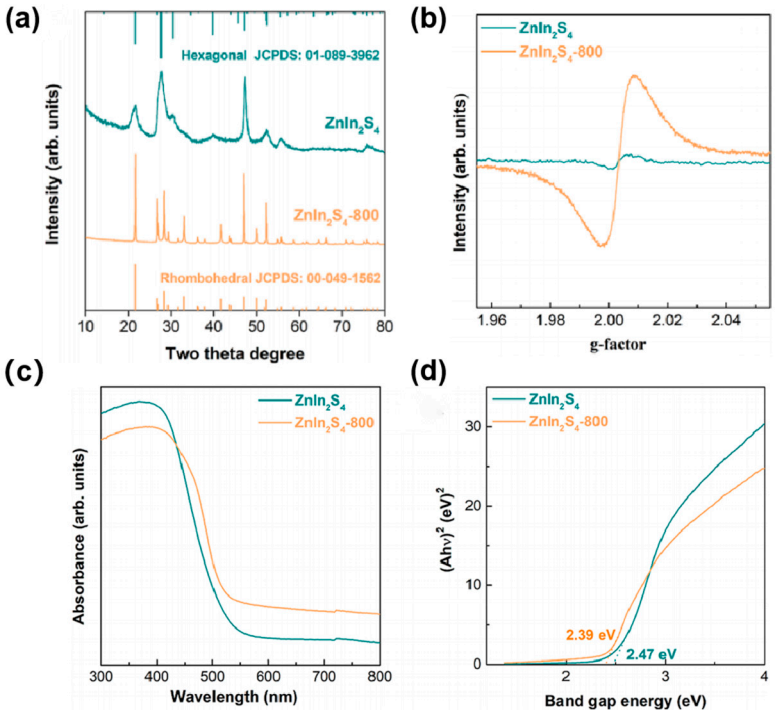

Figure 3. (**a**) X-ray diffraction (XRD) patterns of $ZnIn_2S_4$ and $ZnIn_2S_4$-800, (**b**) Electron paramagnetic resonance (EPR) results of $ZnIn_2S_4$ and $ZnIn_2S_4$-800, and (**c**) Ultraviolet–visible (UV−vis) light absorption spectra and (**d**) Band-gap energies of $ZnIn_2S_4$ and $ZnIn_2S_4$-800 [75].

In summary, the introduction of appropriate vacancies in $ZnIn_2S_4$-based photocatalytic materials can narrow the band gap and improve visible-light absorption, increase the charge density of photogenerated carriers and the rate of migration of photogenerated charge separation, and regulate the electronic structure of the material, providing an abundance of surface-active sites and effectively modulating the crystal and energy band structure of the material, thus effectively improving the photocatalytic activity of the material.

4.2. Construction of Heterogeneous Junctions

The construction of heterojunctions from two or more semiconductors is a better modification strategy due to the strong Coulombic forces on the photogenerated charges of a single semiconductor, which are prone to recombination and result in poor photocatalytic activity. The construction of heterojunctions not only improves the photoresponse range of the material, provides a larger specific surface area, exposes more active sites, and modulates the catalyst to form unique structures, but also increases the photogenerated carrier separation and migration rates [76,77]. Depending on the energy band structure of the semiconductor and the photogenerated carrier transfer path, heterojunctions can be classified into six categories: type I heterojunction, type II heterojunction, Schottky junction, p–n heterojunction, Z-scheme heterojunction, and S-scheme heterojunction. The construction of a heterojunction by coupling $ZnIn_2S_4$ with another semiconductor is one of the effective modification methods to overcome the disadvantages of $ZnIn_2S_4$-based photocatalysts such as slow photogenerated charge separation and migration, and easy recombination [78,79]. Therefore, it is important to design and prepare heterojunctions with an appropriate energy band structure and well-matched geometry. In recent years, the photocatalytic performance of heterojunction materials constructed from metal oxides, carbon nitride, and $ZnIn_2S_4$ has been improved to varying degrees and applied in the field of environmental energy [80–84]. Currently, the most widely used in photocatalytic overall water splitting are Z-scheme heterojunctions and Schottky heterojunctions.

4.2.1. Z-Scheme Heterojunction

Most semiconductor materials are unable to achieve one-step photo-excited overall water splitting, due to drawbacks such as the lack of a suitable energy band structure and severe photogenerated carrier complexation. In recent years, the use of two-step photoexcitation, coupling two or more semiconductors to construct a Z-scheme heterojunction, has been widely used to improve the photocatalytic activity of $ZnIn_2S_4$-based photocatalysts with good results [85,86]. There are two main types of Z-scheme heterojunctions: (1) Indirect Z-scheme heterojunctions in which the two semiconductors are not in contact and the charge is transferred through a charge transfer medium such as Au and graphene; (2) a direct Z-scheme heterojunction in which two semiconductors come into contact, generating an electric field at the inner boundary due to differences in the work function and Fermi energy levels, accelerating the separation of photogenerated carriers [87,88]. The construction of Z-scheme heterojunctions facilitates the spatial separation of photogenerated charges, inhibits recombination, and maintains the high redox capacity of the material, effectively improving photocatalytic activity.

Indirect Z-Scheme Heterojunction

In 2017, Zhong et al. reported an indirect Z-scheme heterojunction material, $ZnIn_2S_4$/RGO/BMO, in which $ZnIn_2S_4$ acts as a hydrogen-depleting photocatalyst, Bi_2MoO_6 (BMO) acts as an oxygen-depleting photocatalyst, and reduced graphene oxide (RGO) acts as an electron mediator (Figure 4a) [89]. They prepared BMO and $ZnIn_2S_4$ by solvent thermal and hydrothermal methods, respectively, and then loaded Pt and CoOx co-catalysts onto $ZnIn_2S_4$ and BMO, respectively, to achieve photocatalytic overall water splitting without sacrificial agents. The construction of Z-scheme heterojunctions and the appropriate number of electron-mediated RGO can effectively increase the photogenerated charge separation and migration rates of the catalysts and improve the photocatalytic activity of the composites. Experiments show that the optimum material is Pt/$ZnIn_2S_4$-RGO (3%)-CoOx/BMO, which achieves a hydrogen yield of 31.4 μmol g^{-1} h^{-1} and an oxygen yield of 15.8 μmol g^{-1} h^{-1} under visible-light irradiation in pure water.

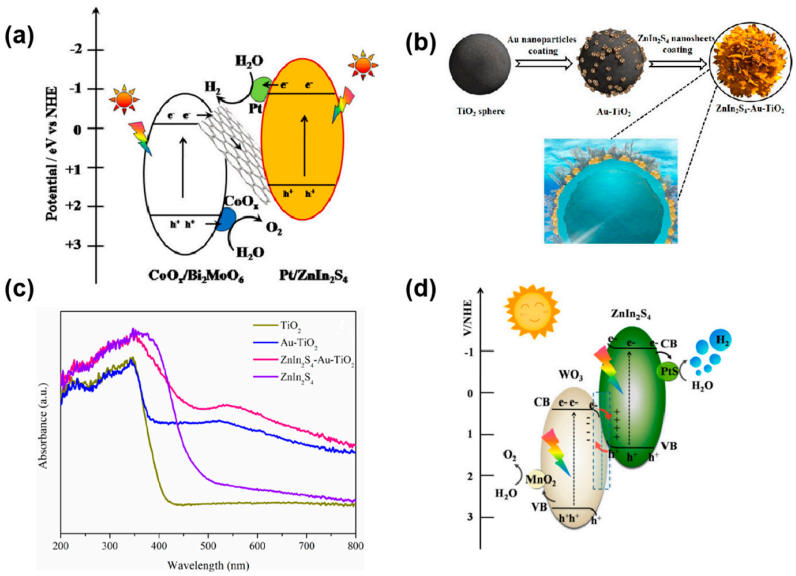

Figure 4. (**a**) Z-scheme photocatalytic water splitting systems consisting of H_2-evolving photocatalyst (Pt/$ZnIn_2S_4$), O_2-evolving photocatalyst (CoOx/BMO), and electron medium (RGO) [89]. (**b**) Schematic illustration of the fabrication process of the $ZnIn_2S_4$-Au-TiO_2 photocatalyst: Au-TiO_2 is prepared by a chemical-deposition process and $ZnIn_2S_4$-Au-TiO_2 is synthesized by the solvothermal process. (**c**) UV-Vis diffuse reflectance spectra of TiO_2, Au-TiO_2, $ZnIn_2S_4$-Au-TiO_2, and $ZnIn_2S_4$ [90]. (**d**) Proposed mechanism for photocatalytic overall water splitting over PtS-$ZnIn_2S_4$/WO_3-MnO_2 nanocomposites under visible light [91].

In 2018, Yang et al. reported a sea-urchin-shaped $ZnIn_2S_4$-based catalyst ($ZnIn_2S_4$-Au-TiO_2), achieving a hydrogen yield of 186.3 μmol g^{-1} h^{-1} and an oxygen yield of 66.3 μmol g^{-1} h^{-1} without co-catalysts and sacrificial agents [90]. They first synthesized TiO_2 microspheres, then synthesized Au-TiO_2 by chemically depositing Au nanoparticles on the TiO_2 surface, and finally prepared the indirect Z-scheme heterojunction material $ZnIn_2S_4$-Au-TiO_2 by direct deposition of $ZnIn_2S_4$ on the Au-TiO_2 surface via a solvothermal method (Figure 4b). The Z-scheme heterojunction can effectively promote the electron–hole pair separation efficiency, and the ultra-thin $ZnIn_2S_4$ nanosheets increase the specific surface area of the material and provide more active sites. As shown in Figure 4c, the ultraviolet–visible (UV-Vis) diffuse reflectance spectra show an increase in the visible absorption capacity of the material due to the surface plasmon resonance of the gold nanoparticles (Au NPs). The composite material promotes the separation of photogenerated carriers and increases the light collection capacity of the material, thus effectively improving the photocatalytic activity of the material.

In 2021, Geng et al. reported a Pt-$ZnIn_2S_4$/RGO/Co_3O_4-$BiVO_4$ (110) photocatalyst [92]. They first prepared $BiVO_4$ by the solvothermal method, RGO/Co_3O_4-$BiVO_4$ (110) by photo-deposition and reduction, and Pt-$ZnIn_2S_4$ by the hydrothermal method and photo-deposition. Finally, they used a self-assembly method to prepare Pt-$ZnIn_2S_4$/RGO/Co_3O_4-$BiVO_4$ (110) Z-scheme photocatalysts for photocatalytic overall water splitting without sacrificial agents. The decagonal $BiVO_4$ can accumulate holes and electrons on the (110) and (040) sides and top surfaces, respectively, allowing effective spatial separation of photogenerated carriers, so the decagonal $BiVO_4$ with the (110) surface can be used as an oxygen production photocatalyst. $ZnIn_2S_4$ was used as a hydrogen production photocatalyst and RGO as an electron mediator to construct Z-scheme heterojunctions with $BiVO_4$ (110). The Z-scheme heterojunction effectively increases the rate of photogenerated charge separation and migration, and the appropriate amount of RGO electron mediators and Pt/Co_3O_4 co-catalyst loading promotes electron transfer. The material achieves a hydrogen yield of 24.5 μmol g^{-1} h^{-1} and an oxygen yield of 11.9 μmol g^{-1} h^{-1} under visible-light irradiation in pure water.

Direct Z-Scheme Heterojunction

In 2019, Ding et al. synthesized PtS-$ZnIn_2S_4$/WO_3-MnO_2 direct Z-scheme heterojunctions, achieving a hydrogen yield of 38.8 μmol g^{-1} h^{-1} and an oxygen yield of 15.7 μmol g^{-1} h^{-1} [91]. They used a hydrothermal method to synthesize orthorhombic $WO_3 \bullet H_2O$ nanoplates, which were dehydrated by solvent heat treatment to transform the orthorhombic phase WO_3 to the hexagonal phase. The self-assembly of hexagonal $ZnIn_2S_4$ nanosheets on the surface of hexagonal WO_3 nanorods to prepare $ZnIn_2S_4$/WO_3, Pt, and MnO_2 were selectively deposited on $ZnIn_2S_4$ and WO_3 to prepare materials for photocatalytic overall water splitting under pure water without sacrificial agents. Self-assembled $ZnIn_2S_4$ on the surface of WO_3 nanorods forms an ohmic contact at the interface and a Z-scheme heterojunction between two semiconductor-matched energy band structures (Figure 4d). The construction of Z-scheme heterojunctions effectively promotes the effective spatial separation of photogenerated charges and maintains the high redox capacity of the original semiconductor, resulting in materials with excellent photocatalytic activity.

In 2020, Zhao et al. prepared $BiVO_4$@$ZnIn_2S_4$/Ti_3C_2 MXene quantum dots (BV@ZIS/TC QDs) with layered core–shell structures by in situ growth combined with a two-step solvothermal strategy [93]. They first synthesized $BiVO_4$ microspheres by the hydrothermal method, on which $ZnIn_2S_4$ nanosheets were grown in situ to form a hierarchical core–shell structure (Figure 5a). A solid contact surface and matching energy band structure was ensured between two semiconductors to construct the Z-scheme heterojunction, and then it was loaded with Ti_3C_2 MXene QDs (TC QDs) as a co-catalyst to synthesize composite material for photocatalytic overall water splitting. Material electron transfer pathways are characterized, $BiVO_4$@$ZnIn_2S_4$ (BV@ZIS) constructs space-charge-separated all-solid z-structures, and co-catalyst TC QDs form Schottky barriers between the interfaces, ef-

fectively promoting photogenerated carrier separation and migration rates (Figure 5b). The unique layered core–shell structure of the material increases light utilization, shortens the charge diffusion distance, increases more active sites, and effectively improves the photocatalytic activity. The material achieves a hydrogen yield of 102.67 μmol g^{-1} h^{-1} and an oxygen yield of 50.83 μmol g^{-1} h^{-1} under visible-light irradiation.

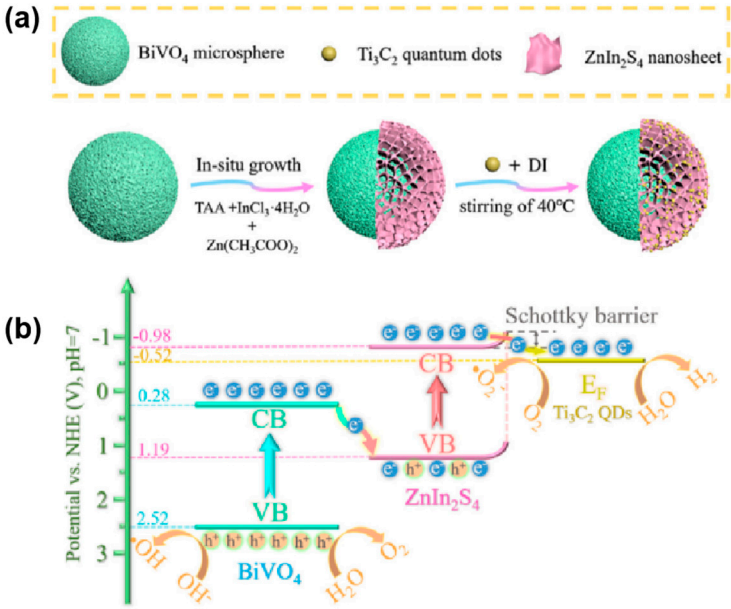

Figure 5. (**a**) Schematic illustration for the formation of BV@ZIS/TC QDs assembly, (**b**) Schematic illustration of band structure and electron–hole transfer mechanism for BV@ZIS/TC QDs [93].

In 2021, Wang et al. reported a Z-scheme heterojunction ZIS-WO/C-wood (Sv-$ZnIn_2S_4$-Ov-WO_3/C-wood) catalyst photothermal integrated system for photocatalytic overall water splitting [94]. They first synthesized sulfur-deficient Pt/Sv-$ZnIn_2S_4$ (Pt/ZIS) by hydrothermal and reduction methods, followed by oxygen-deficient WO_3 (WO) by solvothermal and calcination methods, and CoOx/WO by loading CoOx. Finally, Pt/ZIS and CoOx/WO were dispersed in water to form a solution and spin-coated onto C-wood, and vacuum-assisted heat treatment was applied to construct a photocatalyst photothermal integration system for photocatalytic overall water splitting. ZIS and WO construct Z-scheme heterojunctions, forming a built-in electric field that effectively improves the efficiency of photogenerated charge separation and migration. The conductive material C-wood can act as an electron transfer medium, facilitating electron transfer, and can also use the photothermal effect to convert liquid water to water vapor, transforming the three-phase into a solid/gas two-phase and lowering the carrier recombination and photocatalytic reaction barrier. The photothermal-assisted Z-scheme heterojunction materials effectively increase the photocatalytic activity, achieving a hydrogen yield of 169.2 μmol g^{-1} h^{-1} and an oxygen yield of 82.5 μmol g^{-1} h^{-1}.

Zuo et al. synthesized TiO_2-$ZnIn_2S_4$ nanoflowers (TNZIS) by integrating ultrathin TiO_2 nanosheets into $ZnIn_2S_4$ growth solutions in 2021 to construct direct Z-scheme heterojunctions for photocatalytic overall water splitting under co-catalyst-free conditions (Figure 6a) [95]. TiO_2 nanosheets (TiO_2 NSs) construct direct Z-scheme heterojunctions with $ZnIn_2S_4$ to enhance the rate of photogenerated charge separation and inhibit recombination. TiO_2 has a larger work function and smaller Fermi energy level than $ZnIn_2S_4$ (Figure 6c), causing electrons from $ZnIn_2S_4$ to tend to flow into TiO_2 to balance the Fermi energy level and bend the energy band, forming a (−)TiO_2/(+)$ZnIn_2S_4$ built-in electric field at the heterojunction interface (Figure 6b,d) and promoting direct Z-scheme heterojunction formation. The introduction of TiO_2 NSs can effectively inhibit the aggregation of $ZnIn_2S_4$ materials and increase the specific surface area and active sites of the materials, thus ef-

fectively improving the photocatalytic activity. The best material, TNZIS-50, produces 214.9 μmol g^{-1} h^{-1} of hydrogen and 81.7 μmol g^{-1} h^{-1} of oxygen.

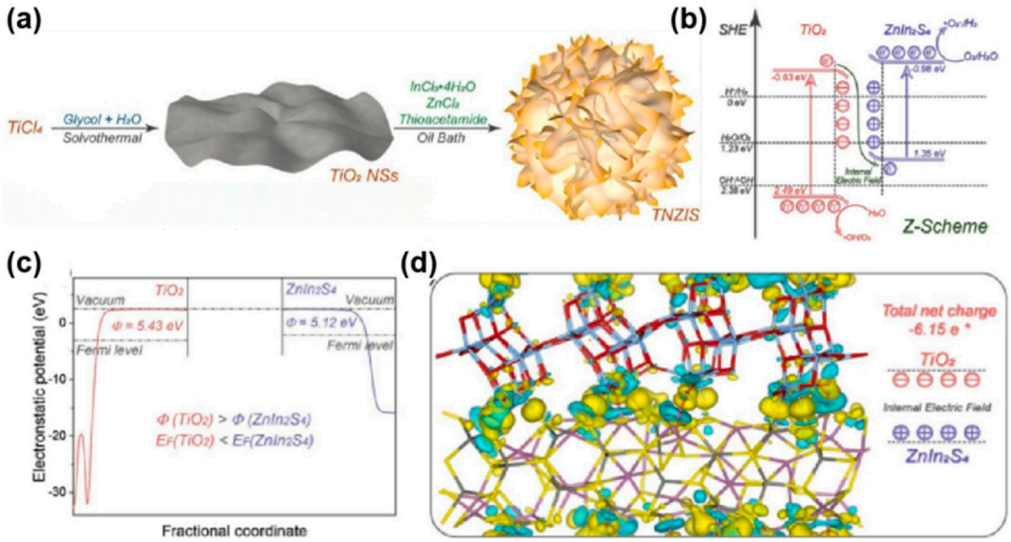

Figure 6. (**a**) Schematic illustration for the synthetic process of TNZIS, (**b**) Schematic illustration for the reaction mechanism of photocatalytic water splitting over direct Z-scheme TNZIS heterojunction, (**c**) Calculated average potential profile along the Z axis of TiO_2 and $ZnIn_2S_4$. (**d**) Difference in charge density isosurface at the interface between TiO_2 and $ZnIn_2S_4$. Ti: blue, O: red, Zn: silver, In: purple, and S: yellow sticks. Blue and yellow areas indicate the loss and accumulation of electrons, respectively. * Total net charge is derived by the sum of Bader atomic charges on the TiO_2 layer. (For interpretation of the references to color in this figure legend, the reader is referred to the web version of this article) [95].

In 2022, Zhang et al. designed and prepared a direct Z-scheme heterojunction $BiFeO_3/ZnIn_2S_4$ with ferroelectric polarization and internal electric field synergy by a two-step solvothermal method to achieve photocatalytic overall water splitting without a co-catalyst [96]. They prepared $BiFeO_3$ by the solvothermal method and then grew ultrathin $ZnIn_2S_4$ nanosheets on $BiFeO_3$ polyhedral particles to prepare $BiFeO_3/ZnIn_2S_4$. Chalcogenide ABO_3-type ferroelectric semiconductors $BiFeO_3$ and $ZnIn_2S_4$ construct Z-scheme heterojunctions. Due to the different Fermi energy levels of $BiFeO_3$ and $ZnIn_2S_4$ forming a built-in electric field, the ferroelectric polarization and internal electric field effectively promote photogenerated carrier migration and separation efficiency. The increased specific surface area and rich pore distribution of the material provide more catalytic active sites, thus effectively increasing the photocatalyst activity and achieving a hydrogen yield of 87.3 μmol g^{-1} h^{-1} and an oxygen yield of 42.3 μmol g^{-1} h^{-1}.

Yang et al. reported a direct Z-scheme heterojunction $BiOBr/ZnIn_2S_4$ (BOB/ZIS) with atomic contact surfaces [97]. They constructed direct Z-scheme heterojunctions with atomic contact surfaces by in situ growth of $ZnIn_2S_4$ nanosheets on the surface of BiOBr nanosheets using a solvothermal method to achieve photocatalytic overall water splitting without sacrificial agents and co-catalysts (Figure 7a). As shown in Figure 7b, the disappearance of the Bi-O peak in X-ray photoelectron spectroscopy (XPS) O 1s and the appearance of Bi-S stretching vibrations in the composite at 1116 cm^{-1} in the FTIR spectrum of BiOBr prove (Figure 7c) that the introduction of TAA into the material during the growth of $ZnIn_2S_4$ breaks the Bi-O bond and forms a Bi-S bond at the heterojunction interface, creating an interface with atomic-level seamlessness. Direct Z-scheme heterojunctions with atomic interfacial connections are effective in increasing the photogenerated charge transfer rate, achieving hydrogen yields of 628 μmol g^{-1} h^{-1} and oxygen yields of 304 μmol g^{-1} h^{-1} under visible-light irradiation in pure water.

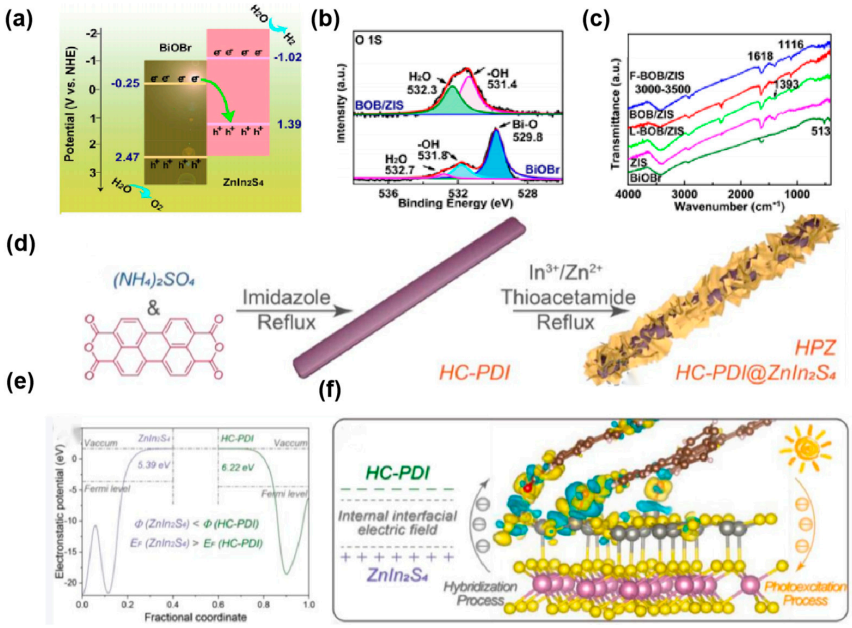

Figure 7. (**a**) Band structures of the BiOBr/$ZnIn_2S_4$ (BOB/ZIS) direct Z-scheme heterojunction; (**b**) X-ray photoelectron spectroscopy (XPS) spectra O 1s; (**c**) FTIR spectra of composite samples [97]. (**d**) Schematic illustration of HPZ synthesis, (**e**) Z axis potential profile of HC-PDI and ZnIn2S4. (**f**) Differential charge density between HC-PDI and ZnIn2S4. Zn: silver, In: purple, S: yellow, C: brown, O: red, and H: white spheres [98].

In 2022, Zuo et al. synthesized an organic–inorganic hybrid material HC-PDI@$ZnIn_2S_4$ OIHs (HPZ) for photocatalytic overall water splitting without co-catalysts and sacrificial agents, achieving hydrogen yields of 275.4 μmol g^{-1} h^{-1} and oxygen yields of 138.4 μmol g^{-1} h^{-1} under visible-light irradiation [98]. They first synthesized the high-crystalline perylene-dicarboximide supramolecule (HC-PDI) with a highly ordered crystal structure and efficient water oxidation activity by nucleophilic addition and self-assembly, and then synthesized organic–inorganic hybrids by lateral epitaxial growth of $ZnIn_2S_4$ nanosheets on highly crystalline HC-PDI nanorods (Figure 7d). As $ZnIn_2S_4$ and HC-PDI have different work functions and Fermi energy levels (Figure 7e), electrons in $ZnIn_2S_4$ will spontaneously transfer to HC-PDI, creating an electron-consuming layer at the internal interface to generate energy band bending and built-in electric fields, building direct Z-scheme heterojunctions. As shown in Figure 7f, the differential charge density between HC-PDI and $ZnIn_2S_4$ can reveal the charge transfer path. The strong covalent coupling between $ZnIn_2S_4$ and HC-PDI provides a fast channel for the charge, and the Z-scheme heterojunction effectively promotes the photogenerated charge separation rate. The proper lateral epitaxial growth of $ZnIn_2S_4$ gives the composite a layered dendritic structure, which facilitates the improvement of the specific surface area, pore size, pore volume, and visible light collection capacity of the material.

In 2023, Zou et al. constructed Z-scheme heterojunctions with $ZnIn_2S_4$ based on the excellent oxidation activity of $InVO_4$ metal oxides [99]. They first synthesized $InVO_4$ nanosheets by the hydrothermal method under acidic conditions, and then formed layered $InVO_4$@$ZnIn_2S_4$ (InVZ) heterojunctions by the in situ growth of $ZnIn_2S_4$ on them by the magnetic stirring reflux oil bath method. The $InVO_4$ work function is greater than that of $ZnIn_2S_4$, causing electrons in $ZnIn_2S_4$ to spontaneously enter $InVO_4$, resulting in the bending of the interfacial energy band within the heterojunction and the formation of (−)$InVO_4$@(+)$ZnIn_2S_4$. The built-in electric field promotes the construction of Z-scheme heterojunctions. The material semiconductor types and the corresponding conduction and valence band positions were demonstrated by characterization of the Mott–Schottky and Tauc energy band gaps of $InVO_4$ and $ZnIn_2S_4$. The construction of $InVO_4$@$ZnIn_2S_4$

Z-scheme heterojunctions is further confirmed by their interleaved energy band structures. The Z-heterojunction of InVZ effectively promotes the separation and migration of photogenerated carriers and maintains the high redox activity of the catalyst. The composite material has a larger surface area and pore volume, providing more active sites, thus effectively improving the overall photocatalytic overall water splitting activity of the material. The optimum material InVZ-90 achieves a hydrogen yield of 153.3 μmol g^{-1} h^{-1} and an oxygen yield of 76.9 μmol g^{-1} h^{-1} under visible light without any co-catalyst.

4.2.2. Schottky Junctions

The Schottky junction is an interface between a metal and a semiconductor. As the metal and semiconductor have different escape work and Fermi energy levels, the Fermi energy level shifts when the metal and semiconductor come into contact until the Fermi energy level equilibrates [100,101]. When the semiconductor is an n-type semiconductor and the metal escape work is greater than the semiconductor Fermi energy level, a Schottky barrier will form at the interface, limiting the flow of electrons from the semiconductor to the metal, inhibiting photogenerated carrier compounding, and effectively improving photocatalytic activity.

In 2021, Cai et al. synthesized a yolk–shell $ZnIn_2S_4$-based photocatalyst $NiCo_2S_4/ZnIn_2S_4/Co_3O_4$ for photocatalytic overall water splitting without sacrificial agents [102]. They first prepared nickel–cobalt-based metal–organic framework (MOF) materials as precursors by the solvothermal method, synthesized yolk–shell $NiCo_2S_4$ (NCS) with semi-metallic properties by sulfidation reaction and heat treatment, then grew $ZnIn_2S_4$ nanosheets in situ on the surface of NCS by low-temperature solvothermal method, and finally decorated Co_3O_4 nanoparticles to prepare photocatalysts (Figure 8a). The characteristic peak of NiCo-glyceric acid disappeared and shifted to $NiCo_2S_4$ when vulcanized at different vulcanization temperatures for 8 h. The precursors were vulcanized at 150, 180, and 210 °C for 8 h to form ball-in-ball hollow spheres, yolk–shell hollow spheres, and a single hollow sphere, respectively, with the yolk–shell structure providing more active sites and improving the photocatalytic activity of the material. As shown in Figure 8b,c, based on the energy band diagrams of $ZnIn_2S_4$ and NCS as well as the energy band diagrams after contact, it is shown that the semi-metallic NCS forms a Schottky-specific heterojunction with $ZnIn_2S_4$ to facilitate charge transfer. The photocatalyst has a unique yolk–shell structure that locates reduction and oxidation sites on the inner and outer surfaces of $ZnIn_2S_4$, respectively, allowing for directional charge separation, inhibition of inverse reactions, and providing more active sites.

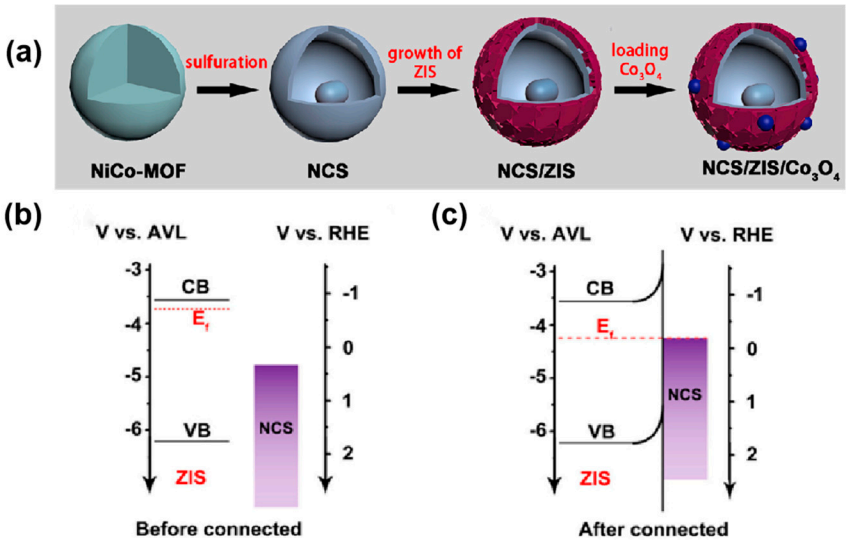

Figure 8. (**a**) Schematic illustration of the synthetic process of $NiCo_2S_4/ZnIn_2S_4/Co_3O_4$ heterostructure, and band alignment of $ZnIn_2S_4$ and $NiCo_2S_4$ before (**b**) and after (**c**) their connection [102].

In 2022, Liu et al. designed and prepared a sandwich structure material Nb_4C_3Tx MXene@$ZnIn_2S_4$-OH by in situ growth and peroxide plasma post-treatment [103]. They first prepared uniformly dispersed accordion-like multilayer Nb_4C_3Tx MXenes by selective chemical etching, then ultrathin $ZnIn_2S_4$ was epitaxially grown on their surface to synthesize the sandwich structure Nb_4C_3Tx MXene@ $ZnIn_2S_4$ at the double heterojunction interface (Figure 9a), followed by a peroxy plasma technique to generate many hydroxyl functional groups to obtain photocatalysts for photocatalytic monolithic water splitting in the absence of sacrificial agents. The work function of $ZnIn_2S_4$ and Nb_4C_3Tx MXene shows that the transfer of electrons from $ZnIn_2S_4$ to Nb_4C_3Tx MXene at the interface causes the $ZnIn_2S_4$ energy band to rise, holes remain in $ZnIn_2S_4$, and the Nb_4C_3Tx MXene@$ZnIn_2S_4$ photocatalyst forms a Schottky junction (Figure 9b,c). The photocatalyst promotes photogenerated carrier transfer and has a larger surface area and pore size and pore volume for rapid adsorption of water molecules. In addition, the OH functional group on the surface of $ZnIn_2S_4$ collects photogenerated holes, and the unique eggshell-type structure of the composite material allows the generated H_2 and O_2 to be distributed internally and externally, achieving spatial separation of photogenerated carriers and suppressing the inverse reaction. The photocatalyst achieves a hydrogen yield of 53.8 μmol g^{-1} h^{-1} and an oxygen yield of 26.7 μmol g^{-1} h^{-1} under visible-light irradiation.

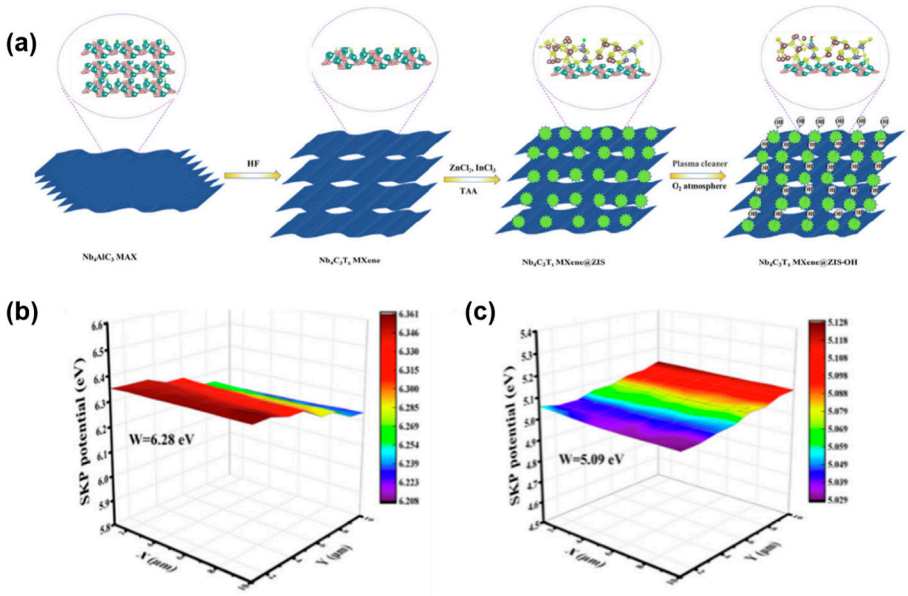

Figure 9. (**a**) Schematic illustration of the synthetic process of Nb_4C_3Tx MXene@ $ZnIn_2S_4$-OH sandwich composite, (**b**) Scanning kelvin probe (SKP) maps of (**c**) Nb_4C_3Tx MXene and $ZnIn_2S_4$ [103].

4.3. Loaded Co-Catalyst

Photocatalytic overall water splitting is mainly based on three basic processes of photocatalysis. The low overall photogenerated charge separation and migration efficiency and the severe compounding of photogenerated charges limit the catalytic photocatalytic activity due to the Coulombic force constraint and the high potential barrier of the transfer process, as well as the unfavorable thermodynamic process of water generation of H_2 and O_2. In this regard, the loading of co-catalysis on semiconductors is a preferable strategy. When a semiconductor is loaded with a co-catalyst, photogenerated electrons and photogenerated holes migrate to the co-catalyst for reduction–oxidation reactions, effectively facilitating photogenerated charge separation and migration. In addition, loaded co-catalysts have the advantage of reducing the activation energy, inhibiting photo-corrosion, and providing an abundance of surface reaction sites [104,105]. Unlike modification strategies such as doping and the construction of heterojunctions, catalysts loaded with co-catalysts can usually be synthesized using photo-deposition.

Suitable co-catalysts are available for both the hydrogen and oxygen production halves of the photocatalytic overall water splitting. The main hydrogen-dissolving co-catalysts are noble metals such as Pt and Au, transition metal monomers such as Co and Ni, transition metal sulfides such as NiP and MoS_2, and phosphides. The main oxygen-dissolving co-catalysts are noble metal oxides such as RuO_2 and IrO_2, and transition metal oxides such as CoOx [106]. In photocatalytic overall water splitting systems, we usually load hydrogen- and oxygen-precipitating co-catalysts onto the catalyst separately to reduce the catalyst surface potential barrier, improve the efficiency of photogenerated charge separation and migration, and better achieve photocatalytic overall water splitting. For example, CdS loaded with Pt and Ru complexes as hydrogen and oxygen production co-catalysts, Mg-doped $BaTaO_2N$ loaded with Cr_2O_3/(Na)Rh and IrO_2 as hydrogen and oxygen production co-catalysts, and Ge_3N_4 loaded with spatially separated mixed cathode and anode co-catalysts, and CoOx-Mo_2N all enable photocatalytic monolithic water splitting [107,108].

The photocatalytic activity can be influenced by adjusting the amount of co-catalyst loading, the type of co-catalyst, the shape of the co-catalyst, etc. In 2023, Jing et al. prepared spatially separated double-coordinated co-catalyst $ZnIn_2S_4$ composites [109]. They first prepared the hexagonal crystalline phase $ZnIn_2S_4$ by the hydrothermal method, and then prepared $ZnIn_2S_4$-Pt-Cr and $ZnIn_2S_4$-Rh-Cr by photo-deposition with Pt-Cr and Rh-Cr co-catalysts loaded on the surface of $ZnIn_2S_4$. The elements Pt and Rh are used as water reduction sites and Cr as water oxidation sites to promote hydrogen and oxygen production reactions, respectively, for overall water splitting. The energy-dispersive X-ray spectroscopy (EDS)-scanned elemental signals of Rh, Cr, and Pt elements at different positions to probe the loading position of the co-catalysts showed that: Pt and Cr elements had consistent signal changes and were hybrids; Rh and Cr elements had different signal changes and achieved spatial separation. In addition, X-ray photoelectron spectroscopy (XPS) demonstrated the formation of Rh-S bonds in the $ZnIn_2S_4$-Rh-Cr material, facilitating the spatial separation of the co-catalyst. The materials loaded with double-assisted catalysts can effectively improve the separation and migration efficiency of photogenerated carriers, inhibit photo-corrosion of the materials, and improve the photocatalytic performance of the materials. The photocatalytic overall water splitting performance of the loaded spatially separated dual-assisted catalyst $ZnIn_2S_4$-Rh-Cr composite was twice that of the $ZnIn_2S_4$-Pt-Cr material, achieving hydrogen yields of 5.9 μmol h^{-1} and oxygen yields of 2.9 μmol h^{-1} at AM 1.5 G. As shown in Table 2, in recent years, researchers have achieved overall water splitting of $ZnIn_2S_4$-based photocatalysts through modification strategies such as doping, vacancies, construction of heterojunctions, and loading of co-catalysts.

Table 2. Summary of reports on photocatalytic overall water splitting of $ZnIn_2S_4$-based catalysts.

Photocatalyst	Cocatalyst	Reaction Systems	Light Source	H_2 (μmol g^{-1} h^{-1})	O_2 (μmol g^{-1} h^{-1})	AQE	Ref.
Ag-$ZnIn_2S_4$	/	12 mg (100 mL H_2O)	300 W Xe lamp (λ > 420 nm)	56.6	29.1	0.70% (405 nm) 0.57% (420 nm) 0.20% (450 nm)	[69]
dZni-$ZnIn_2S_4$	/	50 mg (120 mL H_2O)	300 W Xe lamp (λ > 420 nm)	42.8	19.1	1.51% (420 nm)	[70]
Al-$ZnIn_2S_4$	/	50 mg (100 mL H_2O)	300 W Xe lamp (λ ≥ 420 nm)	77.2	35.3	1.61% (420 nm)	[71]
Sv-$ZnIn_2S_4$-O ($ZnIn_2S_4$-350 °C-4 h)	Pt/Cr	50 mg (100 mL H_2O)	300 W Xe lamp (λ ≥ 420 nm)	270.2	130.0	0.21% (420 nm)	[72]
Sv-$ZnIn_2S_4$ ($ZnIn_2S_4$-800)	Pt/Cr	50 mg (100 mL H_2O)	300 W Xe lamp (λ ≥ 420 nm)	68.0	31.0	0.041% (420 nm) 0.016% (450 nm) 0.004% (500 nm)	[75]
$ZnIn_2S_4$/RGO/BMO	Pt/CoOx	100 mg (100 mL H_2O)	200 W Xe lamp (λ > 420 nm)	31.4	15.8	/	[89]
$ZnIn_2S_4$-Au-TiO_2	/	50 mg (100 mL H_2O)	300 W Xe lamp	186.3	66.3	/	[90]

Table 2. *Cont.*

Photocatalyst	Cocatalyst	Reaction Systems	Light Source	H_2 (μmol g^{-1} h^{-1})	O_2 (μmol g^{-1} h^{-1})	AQE	Ref.
Pt-$ZnIn_2S_4$/RGO/Co_3O_4-$BiVO_4$(110)	Pt/Co_3O_4	50 mg (100 mL H_2O)	300 W Xe lamp (λ > 420 nm)	24.5	11.9	/	[92]
PtS-$ZnIn_2S_4$/WO_3-MnO_2	Pt/MnO_2	50 mg (100 mL H_2O)	300 W Xe lamp (λ > 420 nm)	38.8	15.7	/	[91]
$BiVO_4$@$ZnIn_2S_4$/Ti_3C_2 MXene QDs	Ti_3C_2 MXene QDs	60 mg (H_2O)	300 W Xe lamp (λ > 400 nm)	102.67	50.83	2.40% (410 nm) 2.90% (460 nm) 1.40% (510 nm) 0.20% (560 nm)	[93]
ZIS-WO/C-wood (Sv-$ZnIn_2S_4$-Ov-WO_3/C-wood)	Pt/CoOx	floated at the water–air interface	300 W Xe lamp (AM 1.5G)	169.2	82.5	/	[94]
TiO_2-$ZnIn_2S_4$	/	20 mg (50 mL H_2O)	300 W Xe lamp	214.9	81.7	/	[95]
$BiFeO_3$/$ZnIn_2S_4$	/	12 mg (100 mL H_2O)	300 W Xe lamp (λ > 420 nm)	87.3	42.3	1.12% (420 nm)	[96]
BiOBr/$ZnIn_2S_4$	Pt	100 mg (100 mL H_2O)	300 W Xe lamp (λ > 420 nm)	628	304	/	[97]
HC-PDI@$ZnIn_2S_4$ OIHs	/	5 mg (50 mL H_2O)	300 W Xe lamp (λ ≥ 400 nm)	275.4	138.4	16.14% (400 nm)	[98]
$InVO_4$@$ZnIn_2S_4$	/	5 mg (50 mL H_2O)	300 W Xe lamp	153.3	76.9	24.28% (365 nm) 19.31% (380 nm) 15.29% (400 nm) 9.75% (420 nm) 6.93% (460 nm)	[99]
$NiCo_2S_4$/$ZnIn_2S_4$/Co_3O_4	$NiCo_2S_4$/Co_3O_4	10 mg (15 mL H_2O)	/	103.3	26.7	/	[102]
Nb_4C_3Tx MXene@$ZnIn_2S_4$-OH	Nb_4C_3Tx MXene/OH	20 mg (100 mL H_2O)	300 W Xe lamp (λ > 420 nm)	53.8	26.7	/	[103]
$ZnIn_2S_4$-Rh-Cr	Rh-Cr	50 mg (100 mL H_2O)	300 W Xe lamp (AM 1.5G)	118	58	0.084% (420 nm) 0.028% (450 nm) 0.017% (500 nm)	[109]

5. Conclusions and Outlook

In a two-carbon context, the use of clean, renewable solar energy is an ideal solution to current energy and environmental problems. Photocatalytic overall water splitting, which produces clean, high-energy-density hydrogen without sacrificial agents, is the ideal, low-cost method for solar–chemical energy conversion in a variety of solar applications. Compared with oxides and nitrides, $ZnIn_2S_4$ as a ternary metal sulfide has the advantages of tunable band gap, satisfying the energy band of photocatalytic overall water splitting, strong photostability, and easy preparation, which makes it a more ideal material for photocatalytic overall water splitting. In this study, we systematically review recent advances in $ZnIn_2S_4$-based photocatalysts for photocatalytic overall water splitting in solar–chemical energy conversion. This study mainly introduces the basic principles of its photocatalytic overall water splitting, the properties of the $ZnIn_2S_4$ photocatalyst, including its crystal configuration and energy band structure, the main synthesis methods, and morphology. It also reviews the research progress of photocatalytic overall water splitting of $ZnIn_2S_4$-based photocatalytic materials, including modification strategies such as elemental doping, vacancy defects, the construction of heterojunctions, and the loading of co-catalysts.

Although good progress has been made in the current study of $ZnIn_2S_4$-based photocatalysts for water splitting, there are still some limitations of $ZnIn_2S_4$-based photocatalysts for water splitting that limit their wide application. The overall photogenerated charge separation and utilization efficiency are low due to the Coulombic force constraint between the photogenerated electrons and holes and the interfacial potential barriers between charge transfers, which are much higher than the photogenerated electrons and holes that they separate and migrate to the redox sites to participate in the reaction. Furthermore, although $ZnIn_2S_4$ has a good light collection capacity, it is mainly responsive to visible light and does not utilize the near-infrared light, which is nearly 50% of solar energy, and the inevitable existence of $ZnIn_2S_4$-based photocatalysts as metal sulfides with their photo-corrosive

fluxes affects their photocatalytic overall water splitting activity. Therefore, more efforts are still needed to make $ZnIn_2S_4$-based photocatalysts better for use in photocatalytic overall water splitting systems:

(1) Building active crystal surfaces. Very few studies have systematically addressed the relationship between the active crystal plane of $ZnIn_2S_4$ photocatalysts and the overall water splitting activity of photocatalysis. Usually, photocatalytic reactions occur on the surface of the material, so the specific surface area of the material and the exposed crystalline surface all affect the catalyst activity. Particularly due to the anisotropy of crystals, different crystal faces have different structures and atomic arrangements and usually exhibit different properties. It is important to clarify the relationship between different crystal types and their different crystal faces and photocatalytic activity, and to explore which crystal exposures alter the conduction/valence band position of the material and enhance electron reduction/hole oxidation, and which crystal exposures accumulate photogenerated charges/holes. Improving the photogenerated charge separation and migration efficiency and reducing photo-corrosion can be achieved by modulating the crystalline surface of $ZnIn_2S_4$-based photocatalysts. Therefore, if the relationship between the different crystalline facets of $ZnIn_2S_4$ and photocatalytic activity can be clarified, we can better design photocatalytic materials with higher activity and significantly improve their photocatalytic overall water splitting performance.

(2) Photothermal assistance for broad spectrum utilization. Most current applications for photocatalytic monolithic water splitting $ZnIn_2S_4$-based materials respond to visible light and largely fail to utilize near-infrared light, which accounts for approximately 50% of sunlight; therefore, expanding the efficiency of light utilization is essential to achieve high-efficiency photocatalytic overall water splitting. Due to the inherent nature of $ZnIn_2S_4$ materials, most current $ZnIn_2S_4$-based photocatalytic overall water splitting systems employ very limited modification strategies such as doping, vacancies, and the construction of heterojunctions to extend the photo-response range. The combination of photothermal assistance with $ZnIn_2S_4$-based photocatalysts is a very promising strategy for enhancing overall water splitting due to the advantages of photothermal catalysis in terms of wider spectral utilization, enhanced free carrier concentration, and promotion of photogenerated carrier separation. Further efforts are still needed to explore the design of photothermal-assisted $ZnIn_2S_4$-based photocatalysts to achieve broad-spectrum photocatalytic total hydrolysis and the development of low-sink cost materials to replace expensive precious metals.

(3) Morphological adjustments. By adjusting the morphology of $ZnIn_2S_4$-based photocatalytic materials, we can increase the specific surface area, pore size, and volume, and increase the active site to improve the light collection capacity, such as hollow structures for broadband absorption and ultra-thin nanosheets to shorten the photogenerated charge migration efficiency. The current sandwich structure and yolk–shell structure in $ZnIn_2S_4$-based photocatalytic overall water splitting applications have spatially separated water redox sites, allowing for directional separation of photogenerated charges, improved photocatalytic activity, as well as a layered core–shell structure to enhance incident light scattering and reflection effects and improve light utilization efficiency. Although the current modified morphologies are all very good at improving the overall photocatalytic overall water splitting activity, there is still room for improvement. Further research is needed to determine whether some of the complex morphological synthesis steps and materials used can be simplified and cost-effective, whether the prepared materials are stable, and whether morphological adjustments can be made to the $ZnIn_2S_4$ native catalyst to achieve single-component photocatalytic overall water splitting.

Author Contributions: Writing—original draft preparation, Y.Y.; visualization, Z.C.; project administration, X.C.; writing—review and editing, W.S. All authors have read and agreed to the published version of the manuscript.

Funding: This research was funded by National Natural Science Foundation of China: 22006057 and 51902140. Thanks to the Instrumental Analysis Center, Jiangsu University of Science and Technology.

Conflicts of Interest: The authors declare no conflict of interest.

References

1. Tao, X.; Zhao, Y.; Wang, S.; Li, C.; Li, R. Recent advances and perspectives for solar-driven water splitting using particulate photocatalysts. *Chem. Soc. Rev.* **2022**, *51*, 3561–3608. [CrossRef] [PubMed]
2. Wang, Q.; Domen, K. Particulate Photocatalysts for Light-Driven Water Splitting: Mechanisms, Challenges, and Design Strategies. *Chem. Rev.* **2020**, *120*, 919–985. [CrossRef] [PubMed]
3. Fujishima, A.; Honda, K. Electrochemical Photolysis of Water at a Semiconductor Electrode. *Nature* **1972**, *238*, 37–38. [CrossRef] [PubMed]
4. Hu, J.; Chen, C.; Zheng, Y.; Zhang, G.; Li, C.M. Spatially Separating Redox Centers on Zlog cheme $ZnIn_2S_4/BiVO_4$ Hierarchical Heterostructure for Highly Efficient Photocatalytic Hydrogen Evolution. *Small* **2020**, *16*, 2002988. [CrossRef]
5. Su, T.; Men, C.; Chen, L.; Chu, B.; Luo, X.; Ji, H.; Chen, J.; Qin, Z. Sulfur Vacancy and Ti_3C_2Tx Cocatalyst Synergistically Boosting Interfacial Charge Transfer in 2D/2D $Ti_3C_2Tx/ZnIn_2S_4$ Heterostructure for Enhanced Photocatalytic Hydrogen Evolution. *Adv. Sci.* **2022**, *9*, 2103715. [CrossRef]
6. Du, C.; Zhang, Q.; Lin, Z.; Yan, B.; Xia, C.; Yang, G. Half-unit-cell $ZnIn_2S_4$ monolayer with sulfur vacancies for photocatalytic hydrogen evolution. *Appl. Catal. B Environ.* **2019**, *248*, 193–201. [CrossRef]
7. Liu, K.; Zhang, B.; Zhang, J.; Lin, W.; Wang, J.; Xu, Y.; Xiang, Y.; Hisatomi, T.; Domen, K.; Ma, G. Synthesis of Narrow-Band-Gap GaN:ZnO Solid Solution for Photocatalytic Overall Water Splitting. *ACS Catal.* **2022**, *12*, 14637–14646. [CrossRef]
8. Zhang, G.G.; Wang, X.C. Oxysulfide Semiconductors for Photocatalytic Overall Water Splitting with Visible Light. *Angew. Chem.-Int. Ed.* **2019**, *58*, 15580–15582. [CrossRef]
9. Gogoi, D.; Shah, A.; Rambabu, P.; Qureshi, M.; Golder, A.; Peela, N. Step-Scheme Heterojunction between CdS Nanowires and Facet-Selective Assembly of MnOx-$BiVO_4$ for an Efficient Visible-Light-Driven Overall Water Splitting. *ACS Appl. Mater. Interfaces* **2021**, *13*, 45475–45487. [CrossRef]
10. Iwashina, K.; Iwase, A.; Ng, Y.H.; Amal, R.; Kudo, A. Z-schematic water splitting into H_2 and O_2 using metal sulfide as a hydrogen-evolving photocatalyst and reduced graphene oxide as a solid-state electron mediator. *J. Am. Chem. Soc.* **2015**, *137*, 604–607. [CrossRef]
11. Hayat, A.; Sohail, M.; Anwar, U.; Taha, T.A.; El-Nasser, K.S.; Alenad, A.M.; Al-Sehemi, A.G.; Alghamdi, N.A.; Al-Hartomy, O.A.; Amin, M.A.; et al. Enhanced photocatalytic overall water splitting from an assembly of donor-π-acceptor conjugated polymeric carbon nitride. *J. Colloid Interface Sci.* **2022**, *624*, 411–422. [CrossRef]
12. Sun, S.; Gao, R.; Liu, X.; Pan, L.; Shi, C.; Jiang, Z.; Zhang, X.; Zou, J.J. Engineering interfacial band bending over bismuth vanadate/carbon nitride by work function regulation for efficient solar-driven water splitting. *Sci. Bull.* **2021**, *67*, 389–397. [CrossRef]
13. Pan, Y.; Yuan, X.; Jiang, L.; Yu, H.; Zhang, J.; Wang, H.; Guan, R.; Zeng, G. Recent advances in synthesis, modification and photocatalytic applications of micro/nano-structured zinc indium sulfide. *Chem. Eng. J.* **2018**, *354*, 407–431. [CrossRef]
14. Zhu, Q.; Xu, Q.; Du, M.; Zeng, X.; Zhong, G.; Qiu, B.; Zhang, J. Recent Progress of Metal Sulfide Photocatalysts for Solar Energy Conversion. *Adv. Mater.* **2022**, *34*, e2202929. [CrossRef]
15. Hao, X.Q.; Zhou, J.; Cui, Z.W.; Wang, Y.C.; Wang, Y.; Zou, Z. Zn-vacancy mediated electron-hole separation in ZnS/g-C_3N_4 heterojunction for efficient visible-light photocatalytic hydrogen production. *Appl. Catal. B Environ.* **2018**, *229*, 41–51. [CrossRef]
16. Xue, S.; Huang, W.; Lin, W.; Xing, W.; Shen, M.; Ye, X.; Liang, X.; Yang, C.; Hou, Y.; Yu, Z. Interfacial engineering of lattice coherency at ZnO-ZnS photocatalytic heterojunctions—ScienceDirect. *Chem Catal.* **2022**, *2*, 125–139. [CrossRef]
17. Yu, J.; Yu, Y.; Peng, Z.; Wei, X.; Bei, C. Morphology-dependent photocatalytic H_2-production activity of CdS. *Appl. Catal. B Environ.* **2014**, *156–157*, 184–191. [CrossRef]
18. Yuan, Y.-J.; Chen, D.; Yu, Z.-T.; Zou, Z.-G. Cadmium sulfide-based nanomaterials for photocatalytic hydrogen production. *J. Mater. Chem. A Mater. Energy Sustain.* **2018**, *6*, 11606–11630. [CrossRef]
19. Ren, Y.; Foo, J.J.; Zeng, D.; Ong, W.J. ZnIn2S4-Based Nanostructures in Artificial Photosynthesis: Insights into Photocatalytic Reduction toward Sustainable Energy Production. *Small Struct.* **2022**, *3*, 2200017. [CrossRef]
20. Chen, K.; Shi, Y.; Shu, P.; Luo, Z.; Shi, W.; Guo, F. Construction of core–shell FeS_2@$ZnIn_2S_4$ hollow hierarchical structure S-scheme heterojunction for boosted photothermal-assisted photocatalytic H_2 production. *Chem. Eng. J.* **2023**, *454*, 140053. [CrossRef]
21. Zhang, G.; Wu, H.; Chen, D.; Li, N.; Xu, Q.; Li, H.; He, J.; Lu, J. A mini-review on $ZnIn_2S_4$-Based photocatalysts for energy and environmental application. *Green Energy Environ.* **2022**, *7*, 176–204. [CrossRef]
22. Chandrasekaran, S.; Yao, L.; Deng, L.; Bowen, C.; Zhang, Y.; Chen, S.; Lin, Z.; Peng, F.; Zhang, P. Recent advances in metal sulfides: From controlled fabrication to electrocatalytic, photocatalytic and photoelectrochemical water splitting and beyond. *Chem. Soc. Rev.* **2019**, *48*, 4178–4280. [CrossRef] [PubMed]
23. Cai, Y.; Shi, Y.; Shi, W.; Bai, S.; Yang, S.; Guo, F. A one-photon excitation pathway in 0D/3D $CoS_2/ZnIn_2S_4$ composite with nanoparticles on micro-flowers structure for boosted visible-light-driven photocatalytic hydrogen evolution. *Compos. Part B Eng.* **2022**, *238*, 109955. [CrossRef]
24. Shi, W.; Hao, C.; Fu, Y.; Guo, F.; Tang, Y.; Yan, X. Enhancement of synergistic effect photocatalytic/persulfate activation for degradation of antibiotics by the combination of photo-induced electrons and carbon dots. *Chem. Eng. J.* **2022**, *433*, 133741. [CrossRef]

25. Liu, C.; Zhang, Q.; Zou, Z. Recent advances in designing $ZnIn_2S_4$-based heterostructured photocatalysts for hydrogen evolution. *J. Mater. Sci. Technol.* **2023**, *139*, 167–188. [CrossRef]
26. Yadav, G.; Ahmaruzzaman, M. Recent progress on synthesis and modifications of $ZnIn_2S_4$ based novel hybrid materials for potential applications. *Mater. Sci. Eng. B* **2023**, *292*, 116418. [CrossRef]
27. Wang, Z.; Li, C.; Domen, K. Recent developments in heterogeneous photocatalysts for solar-driven overall water splitting. *Chem. Soc. Rev.* **2019**, *48*, 2109–2125. [CrossRef]
28. He, R.; Ran, J. Dilemma faced by photocatalytic overall water splitting. *J. Mater. Sci. Technol.* **2023**, *157*, 107–109. [CrossRef]
29. Navalon, S.; Dhakshinamoorthy, A.; Alvaro, M.; Ferrer, B.; Garcia, H. Metal-Organic Frameworks as Photocatalysts for Solar-Driven Overall Water Splitting. *Chem. Rev.* **2023**, *123*, 445–490. [CrossRef]
30. Bie, C.; Wang, L.; Yu, J. Challenges for photocatalytic overall water splitting. *Chem* **2022**, *8*, 1567–1574. [CrossRef]
31. Huang, Y.; Li, D.; Feng, S.; Jia, Y.; Guo, S.; Wu, X.; Chen, M.; Shi, W. Pt Atoms/Clusters on Ni-phytate-sensitized Carbon Nitride for Enhanced NIR-light-driven Overall Water Splitting beyond 800 nm. *Angew. Chem. Int. Ed. Engl.* **2022**, *61*, e202212234. [CrossRef]
32. Zhou, P.; Navid, I.A.; Ma, Y.; Xiao, Y.; Wang, P.; Ye, Z.; Zhou, B.; Sun, K.; Mi, Z. Solar-to-hydrogen efficiency of more than 9% in photocatalytic water splitting. *Nature* **2023**, *613*, 66–70. [CrossRef]
33. Hu, L.; Huang, J.; Wang, J.; Jiang, S.; Sun, C.; Song, S. Efficiently photocatalytic H_2O overall splitting within the strengthened polarized field by reassembling surface single atoms. *Appl. Catal. B Environ.* **2023**, *320*, 121945. [CrossRef]
34. Chen, J.; Xin, F.; Yin, X.; Xiang, T.; Wang, Y. Synthesis of hexagonal and cubic $ZnIn_2S_4$ nanosheets for the photocatalytic reduction of CO_2 with methanol. *RSC Adv.* **2015**, *5*, 3833–3839. [CrossRef]
35. Lee, J.; Kim, H.; Lee, T.; Jang, W.; Lee, K.H.; Soon, A. Revisiting Polytypism in Hexagonal Ternary Sulfide $ZnIn_2S_4$ for Photocatalytic Hydrogen Production within the Z-Scheme. *Chem. Mater.* **2019**, *31*, 9148–9155. [CrossRef]
36. Yue, Y.; Zou, J. One-step hydrothermal synthesis of rhombohedral $ZnIn_2S_4$ with high visible photocatalytic activity for aqueous pollutants removal. *J. Colloid Interface Sci.* **2023**, *640*, 270–280. [CrossRef]
37. Shen, S.; Guo, P.; Zhao, L.; Du, Y.; Guo, L. Insights into photoluminescence property and photocatalytic activity of cubic and rhombohedral $ZnIn_2S_4$. *J. Solid State Chem.* **2011**, *184*, 2250–2256. [CrossRef]
38. Wang, J.; Sun, S.; Zhou, R.; Li, Y.; He, Z.; Ding, H.; Chen, D.; Ao, W. A review: Synthesis, modification and photocatalytic applications of $ZnIn_2S_4$. *J. Mater. Sci. Technol.* **2021**, *78*, 1–19. [CrossRef]
39. Guo, X.; Liu, X.; Wang, M.; Yan, J.; Chen, Y.; Liu, S. Unveiling the Origin of Co_3O_4 Quantum Dots for Photocatalytic Overall Water Splitting. *Small* **2023**, *19*, e2206695. [CrossRef]
40. Peng, S.; Li, L.; Wu, Y.; Jia, L.; Tian, L.; Srinivasan, M.; Ramakrishna, S.; Yan, Q.; Mhaisalkar, S.G. Size- and shape-controlled synthesis of $ZnIn_2S_4$ nanocrystals with high photocatalytic performance. *CrystEngComm* **2013**, *15*, 1922–1930. [CrossRef]
41. Shi, L.; Yin, P.; Dai, Y. Synthesis and photocatalytic performance of $ZnIn_2S_4$ nanotubes and nanowires. *Langmuir* **2013**, *29*, 12818–12822. [CrossRef] [PubMed]
42. Ambrosi, A.; Pumera, M. Templated Electrochemical Fabrication of Hollow Molybdenum Sulfide Microstructures and Nanostructures with Catalytic Properties for Hydrogen Production. *ACS Catal.* **2016**, *6*, 3985–3993. [CrossRef]
43. Luo, R.-B.; Liu, Q.-J.; Fan, D.-H.; Liu, Z.-T. First-principles calculations to investigate structural, electronic and optical properties of two-dimensional $ZnIn_2S_4$. *Appl. Surf. Sci.* **2022**, *605*, 154739. [CrossRef]
44. Zhang, S.; Liu, X.; Liu, C.; Luo, S.; Wang, L.; Cai, T.; Zeng, Y.; Yuan, J.; Dong, W.; Pei, Y.; et al. MoS_2 Quantum Dot Growth Induced by S Vacancies in a $ZnIn_2S_4$ Monolayer: Atomic-Level Heterostructure for Photocatalytic Hydrogen Production. *ACS Nano* **2018**, *12*, 751–758. [CrossRef] [PubMed]
45. Shen, J.; Zai, J.; Yuan, Y.; Qian, X. 3D hierarchical $ZnIn_2S_4$: The preparation and photocatalytic properties on water splitting. *Int. J. Hydrogen Energy* **2012**, *37*, 16986–16993. [CrossRef]
46. Hu, X.; Yu, J.C.; Gong, J.; Li, Q. Rapid Mass Production of Hierarchically Porous $ZnIn_2S_4$ Submicrospheres via a Microwave-Solvothermal Process. *Cryst. Growth Des.* **2007**, *7*, 2444–2448. [CrossRef]
47. Fang, F.; Chen, L.; Chen, Y.B.; Wu, L.M. Synthesis and Photocatalysis of $ZnIn_2S_4$ Nano/Micropeony. *J. Phys. Chem. C* **2010**, *114*, 2393–2397. [CrossRef]
48. Zhang, E.; Zhu, Q.; Huang, J.; Liu, J.; Tan, G.; Sun, C.; Li, T.; Liu, S.; Li, Y.; Wang, H.; et al. Visually resolving the direct Z-scheme heterojunction in CdS@$ZnIn_2S_4$ hollow cubes for photocatalytic evolution of H_2 and H_2O_2 from pure water. *Appl. Catal. B Environ.* **2021**, *293*, 120213. [CrossRef]
49. Chaudhari, N.S.; Warule, S.S.; Kale, B.B. Architecture of rose and hollow marigold-like $ZnIn_2S_4$ flowers: Structural, optical and photocatalytic study. *RSC Adv.* **2014**, *4*, 12182–12187. [CrossRef]
50. Chen, Z.X.; Li, D.Z.; Zhang, W.J.; Chen, C.; Li, W.J.; Sun, M.; He, Y.H.; Fu, X.Z. Low-Temperature and Template-Free Synthesis of $ZnIn_2S_4$ Microspheres. *Inorg. Chem.* **2010**, *40*, 9766–9772. [CrossRef]
51. Ding, S.; Liu, X.; Shi, Y.; Liu, Y.; Zhou, T.; Guo, Z.; Hu, J. Generalized Synthesis of Ternary Sulfide Hollow Structures with Enhanced Photocatalytic Performance for Degradation and Hydrogen Evolution. *ACS Appl. Mater. Interfaces* **2018**, *10*, 17911–17922. [CrossRef] [PubMed]
52. Gou, X.; Cheng, F.; Shi, Y.; Zhang, L.; Shen, P. Shape-controlled synthesis of ternary chalcogenide $ZnIn_2S_4$ and $CuIn(S,Se)_2$ nano-/microstructures via facile solution route. *J. Am. Chem. Soc.* **2006**, *128*, 7222–7229. [CrossRef] [PubMed]

53. Chen, Y.; Huang, R.; Chen, D.; Wang, Y.; Liu, W.; Li, X.; Li, Z. Exploring the different photocatalytic performance for dye degradations over hexagonal $ZnIn_2S_4$ microspheres and cubic $ZnIn_2S_4$ nanoparticles. *ACS Appl. Mater. Interfaces* **2012**, *4*, 2273–2279. [CrossRef] [PubMed]
54. Yin, X.; Lv, B.; Kang, Y.; Xu, X.; Lei, X.; Li, L.; Wang, H.; Xi, H.; Yang, J.; Yang, Z. Solvent-Induced $ZnIn_2S_4$ Nanosheets Self-assembled Micro-Flowers to Boosting the Photocatalytic Semi-dehydrogenation of 1,2,3,4-Tetrahydroisoquinoline. *Catal. Lett.* **2022**, *153*, 570–583. [CrossRef]
55. Zou, P.; Su, G.; Li, Z.; Li, Y.; Zhou, T.; Kang, Y. Oxalic acid modified hexagonal $ZnIn_2S_4$ combined with bismuth oxychloride to fabricate a hierarchical dual Z-scheme heterojunction: Accelerating charge transfer to improve photocatalytic activity. *Colloids Surf. A Physicochem. Eng. Asp.* **2022**, *633*, 127835. [CrossRef]
56. Su, L.; Ye, X.; Meng, S.; Fu, X.; Chen, S. Effect of different solvent on the photocatalytic activity of $ZnIn_2S_4$ for selective oxidation of aromatic alcohols to aromatic aldehydes under visible light irradiation. *Appl. Surf. Sci.* **2016**, *384*, 161–174. [CrossRef]
57. Shen, S.; Zhao, L.; Guo, L. Morphology, structure and photocatalytic performance of $ZnIn_2S_4$ synthesized via a solvothermal/hydrothermal route in different solvents. *J. Phys. Chem. Solids* **2008**, *69*, 2426–2432. [CrossRef]
58. Salavati-Niasari, M.; Ranjbar, M.; Sabet, M. Synthesis and Characterization of $ZnIn_2S_4$ Nanoparticles by a Facile Microwave Approach. *J. Inorg. Organomet. Polym. Mater.* **2012**, *23*, 452–457. [CrossRef]
59. Yang, W.; Liu, B.; Fang, T.; Jennifer, W.A.; Christophe, L.; Li, Z.; Zhang, X.; Jiang, X. Layered crystalline $ZnIn_2S_4$ nanosheets: CVD synthesis and photo-electrochemical properties. *Nanoscale* **2016**, *8*, 18197–18203. [CrossRef]
60. Hemalatha, S.; Illakkiya, J.T.; Oommen, R.; Rajalakshmi, P.U. Marigold microstructure of zinc thioindate ($ZnIn_2S_4$) thin film—Characteristics. *Optik* **2016**, *127*, 3858–3861. [CrossRef]
61. Huang, J.; Cheuk, W.; Wu, Y.; Lee, F.; Ho, W. Template-free synthesis of ternary sulfides submicrospheres as visible light photocatalysts by ultrasonic spray pyrolysis. *Catal. Sci. Technol.* **2012**, *2*, 1825. [CrossRef]
62. Cadiş, A.I.; Mureșan, L.E.; Perhaița, I.; Pop, L.C.; Saszet, K.; Barbu-Tudoran, L.; Borodi, G. Peculiarities on methyl orange adsorption by porous $ZnIn_2S_4$ prepared in different conditions. *J. Nanoparticle Res.* **2022**, *24*, 1–13. [CrossRef]
63. Zhang, Y.C.; Afzal, N.; Pan, L.; Zhang, X.; Zou, J.J. Structure-Activity Relationship of Defective Metal-Based Photocatalysts for Water Splitting: Experimental and Theoretical Perspectives. *Adv. Sci.* **2019**, *6*, 1900053. [CrossRef]
64. Su, Z.; Fang, F.; Li, X.; Han, W.; Liu, X.; Chang, K. Synergistic surface oxygen defect and bulk Ti^{3+} defect engineering on $SrTiO_3$ for enhancing photocatalytic overall water splitting. *J. Colloid Interface Sci.* **2022**, *626*, 662–673. [CrossRef]
65. Jiang, L.; Yuan, X.; Pan, Y.; Liang, J.; Zeng, G.; Wu, Z.; Wang, H. Doping of graphitic carbon nitride for photocatalysis: A reveiw. *Appl. Catal. B Environ.* **2017**, *217*, 388–406. [CrossRef]
66. Ma, J.; Long, R.; Liu, D.; Low, J.; Xiong, Y. Defect Engineering in Photocatalytic Methane Conversion. *Small Struct.* **2021**, *3*, 2100147. [CrossRef]
67. Patnaik, P. Recent advances in anion doped g-C_3N_4 photocatalysts: A review. *Carbon* **2021**, *172*, 682–711. [CrossRef]
68. Yang, R.; Mei, L.; Fan, Y.; Zhang, Q.; Zhu, R.; Amal, R.; Yin, Z.; Zeng, Z. $ZnIn_2S_4$-Based Photocatalysts for Energy and Environmental Applications. *Small Methods* **2021**, *5*, e2100887. [CrossRef]
69. Pan, R.; Hu, M.; Liu, J.; Li, D.; Wan, X.; Wang, H.; Li, Y.; Zhang, X.; Wang, X.; Jiang, J.; et al. Two-Dimensional All-in-One Sulfide Monolayers Driving Photocatalytic Overall Water Splitting. *Nano Lett.* **2021**, *21*, 6228–6236. [CrossRef]
70. Sun, B.; Bu, J.; Chen, X.; Fan, D.; Li, S.; Li, Z.; Zhou, W.; Du, Y. In-situ interstitial zinc doping-mediated efficient charge separation for $ZnIn_2S_4$ nanosheets visible-light photocatalysts towards optimized overall water splitting. *Chem. Eng. J.* **2022**, *435*, 135074. [CrossRef]
71. Sun, B.; Fan, D.; Chen, X.; Li, Z.; Zhou, W.; Du, Y. Heteroatom-induced domain electrostatic potential difference in $ZnIn_2S_4$ nanosheets for efficient charge separation and boosted photocatalytic overall water splitting. *Mater. Chem. Front.* **2022**, *6*, 1795–1802. [CrossRef]
72. Jing, H.; Ren, J.; Yue, J.; Liu, S.; Liang, Q.; Wu, R.; Wang, Y.; Fang, Z.; Li, H.; Wei, S. $ZnIn_2S_4$ with oxygen atom doping and surface sulfur vacancies for overall water splitting under visible light irradiation. *Catal. Sci. Technol.* **2023**, *13*, 226–232. [CrossRef]
73. Zhang, S.; Yi, X.; Hu, G.; Chen, M.; Shen, H.; Li, B.; Yang, L.; Dai, W.; Zou, J.; Luo, S. Configuration regulation of active sites by accurate doping inducing self-adapting defect for enhanced photocatalytic applications: A review. *Coord. Chem. Rev.* **2023**, *478*, 214970. [CrossRef]
74. He, J.; Hu, L.; Shao, C.; Jiang, S.; Sun, C.; Song, S. Photocatalytic H_2O Overall Splitting into H_2 Bubbles by Single Atomic Sulfur Vacancy CdS with Spin Polarization Electric Field. *ACS Nano* **2021**, *15*, 18006–18013. [CrossRef]
75. Jing, H.; Xu, G.; Yao, B.; Ren, J.; Wang, Y.; Fang, Z.; Liang, Q.; Wu, R.; Wei, S. Sulfur Vacancy-Enriched Rhombohedral $ZnIn_2S_4$ Nanosheets for Highly Efficient Photocatalytic Overall Water Splitting under Visible Light Irradiation. *ACS Appl. Energy Mater.* **2022**, *5*, 10187–10195. [CrossRef]
76. Abdul Nasir, J.; Munir, A.; Ahmad, N.; Haq, T.U.; Khan, Z.; Rehman, Z. Photocatalytic Z-Scheme Overall Water Splitting: Recent Advances in Theory and Experiments. *Adv. Mater.* **2021**, *33*, 2105195. [CrossRef]
77. Lu, C.; Guo, F.; Yan, Q.; Zhang, Z.; Li, D.; Wang, L.; Zhou, Y. Hydrothermal synthesis of type II $ZnIn_2S_4/BiPO_4$ heterojunction photocatalyst with dandelion-like microflower structure for enhanced photocatalytic degradation of tetracycline under simulated solar light. *J. Alloys Compd.* **2019**, *811*, 151976. [CrossRef]
78. Shi, Y.; Li, L.; Xu, Z.; Guo, F.; Shi, W. Construction of full solar-spectrum available S-scheme heterojunction for boosted photothermal-assisted photocatalytic H_2 production. *Chem. Eng. J.* **2023**, *459*, 151976. [CrossRef]

79. Wang, J.; Shi, Y.; Sun, H.; Shi, W.; Guo, F. Fabrication of $Bi_4Ti_3O_{12}/ZnIn_2S_4$ S-scheme heterojunction for achieving efficient photocatalytic hydrogen production. *J. Alloys Compd.* **2023**, *930*, 167450. [CrossRef]
80. Shi, W.; Guo, F.; Li, M.; Shi, Y.; Shi, M.; Yan, C. Constructing 3D sub-micrometer CoO octahedrons packed with layered MoS_2 shell for boosting photocatalytic overall water splitting activity. *Appl. Surf. Sci.* **2019**, *473*, 928–933. [CrossRef]
81. Guo, F.; Huang, X.; Chen, Z.; Sun, H.; Chen, L. Anchoring CoP nanoparticles on the octahedral CoO by self-phosphating for enhanced photocatalytic overall water splitting activity under visible light. *Chin. J. Chem. Eng.* **2021**, *40*, 114–123. [CrossRef]
82. Shi, W.; Li, M.; Huang, X.; Ren, H.; Yan, C.; Guo, F. Facile synthesis of 2D/2D $Co_3(PO_4)_2$/g-C_3N_4 heterojunction for highly photocatalytic overall water splitting under visible light. *Chem. Eng. J.* **2020**, *382*, 122960. [CrossRef]
83. Chen, Z.; Guo, F.; Sun, H.; Shi, Y.; Shi, W. Well-designed three-dimensional hierarchical hollow tubular g-$C_3N_4/ZnIn_2S_4$ nanosheets heterostructure for achieving efficient visible-light photocatalytic hydrogen evolution. *J. Colloid Interface Sci.* **2022**, *607*, 1391–1401. [CrossRef]
84. Guo, F.; Huang, X.; Chen, Z.; Shi, Y.; Sun, H.; Cheng, X.; Shi, W.; Chen, L. Formation of unique hollow $ZnSnO_3$@$ZnIn_2S_4$ core-shell heterojunction to boost visible-light-driven photocatalytic water splitting for hydrogen production. *J. Colloid Interface Sci.* **2021**, *602*, 889–897. [CrossRef]
85. Di, T.; Xu, Q.; Ho, W.; Tang, H.; Xiang, Q.; Yu, J. Review on Metal Sulphide-based Z-scheme Photocatalysts. *ChemCatChem* **2019**, *11*, 1394–1411. [CrossRef]
86. Shi, W.; Hao, C.; Shi, Y.; Guo, F.; Tang, Y. Effect of different carbon dots positions on the transfer of photo-induced charges in type I heterojunction for significantly enhanced photocatalytic activity. *Sep. Purif. Technol.* **2023**, *304*, 122337. [CrossRef]
87. Xu, Q.; Zhang, L.; Yu, J.; Wageh, S.; Al-Ghamdi, A.A.; Jaroniec, M. Direct Z-scheme photocatalysts: Principles, synthesis, and applications. *Mater. Today* **2018**, *21*, 1042–1063. [CrossRef]
88. Xu, Z.; Shi, W.; Shi, Y.; Sun, H.; Li, L.; Guo, F.; Wen, H. Carbon dots as solid-state electron mediator and electron acceptor in S-scheme heterojunction for boosted photocatalytic hydrogen evolution. *Appl. Surf. Sci.* **2022**, *595*, 153482. [CrossRef]
89. Wan, S.; Ou, M.; Zhong, Q.; Zhang, S.; Song, F. Construction of Z-scheme photocatalytic systems using $ZnIn_2S_4$, CoO_x-loaded Bi_2MoO_6 and reduced graphene oxide electron mediator and its efficient nonsacrificial water splitting under visible light. *Chem. Eng. J.* **2017**, *325*, 690–699. [CrossRef]
90. Yang, G.; Ding, H.; Chen, D.; Feng, J.; Hao, Q.; Zhu, Y. Construction of urchin-like $ZnIn_2S_4$-Au-TiO_2 heterostructure with enhanced activity for photocatalytic hydrogen evolution. *Appl. Catal. B Environ.* **2018**, *234*, 260–267. [CrossRef]
91. Ding, Y.; Wei, D.; He, R.; Yuan, R.; Xie, T.; Li, Z. Rational design of Z-scheme PtS-$ZnIn_2S_4/WO_3$-MnO_2 for overall photo-catalytic water splitting under visible light. *Appl. Catal. B Environ.* **2019**, *258*, 117948. [CrossRef]
92. Ou, M.; Li, J.; Geng, M.; Wang, J.; Wan, S.; Zhong, Q. Construction of Z-scheme Photocatalyst Containing $ZnIn_2S_4$, Co_3O_4-Photodeposited $BiVO_4$ (110) Facets and rGO Electron Mediator for Overall Water Splitting into H_2 and O_2. *Catal. Lett.* **2021**, *151*, 2570–2582. [CrossRef]
93. Du, X.; Zhao, T.; Xiu, Z.; Xing, Z.; Li, Z.; Pan, K.; Yang, S.; Zhou, W. $BiVO_4$@$ZnIn_2S_4/Ti_3C_2$ MXene quantum dots assembly all-solid-state direct Z-Scheme photocatalysts for efficient visible-light-driven overall water splitting. *Appl. Mater. Today* **2020**, *20*, 100719. [CrossRef]
94. Wang, Y.; Huang, W.; Guo, S.; Xin, X.; Zhang, Y.; Guo, P.; Tang, S.; Li, X. Sulfur-Deficient $ZnIn_2S_4$/Oxygen-Deficient WO_3 Hybrids with Carbon Layer Bridges as a Novel Photothermal/Photocatalytic Integrated System for Z-Scheme Overall Water Splitting. *Adv. Energy Mater.* **2021**, *11*, 2102452. [CrossRef]
95. Zuo, G.; Wang, Y.; Teo, W.L.; Xian, Q.; Zhao, Y. Direct Z-scheme TiO_2–$ZnIn_2S_4$ nanoflowers for cocatalyst-free photocatalytic water splitting. *Appl. Catal. B Environ.* **2021**, *291*, 120126. [CrossRef]
96. Zhang, J.; Zhang, Y.; Li, L.; Yan, W.; Wang, H.; Mao, W.; Cui, Y.; Li, Y.; Zhu, X. Synergizing the internal electric field and ferroelectric polarization of the $BiFeO_3/ZnIn_2S_4$ Z-scheme heterojunction for photocatalytic overall water splitting. *J. Mater. Chem. A* **2023**, *11*, 434–446. [CrossRef]
97. Yang, Y.; Sun, Z.; Liu, C.; Wang, J.; Qiu, M.; Yan, G.; Zhang, K. Boosting Photocatalytic Overall Water Splitting on Direct Z-Scheme BiOBr/$ZnIn_2S_4$ Heterostructure by Atomic-Level Interfacial Charge Transport Modulation. *ACS Appl. Energy Mater.* **2022**, *5*, 15559–15565. [CrossRef]
98. Zuo, G.; Chen, W.; Yin, Z.; Ma, S.; Wang, Y.; Ji, Q.; Xian, Q.; Yang, S.; He, H. Covalency dominating Z-scheme perylene-dicarboximide@$ZnIn_2S_4$ organic-inorganic hybrids for overall water splitting. *Chem. Eng. J.* **2023**, *456*, 141096. [CrossRef]
99. Zuo, G.; Ma, S.; Yin, Z.; Chen, W.; Wang, Y.; Ji, Q.; Xian, Q.; Yang, S.; He, H. Z-Scheme Modulated Charge Transfer on $InVO_4$@$ZnIn_2S_4$ for Durable Overall Water Splitting. *Small* **2023**, *19*, e2207031. [CrossRef]
100. Li, X.H.; Antonietti, M. Metal nanoparticles at mesoporous N-doped carbons and carbon nitrides: Functional Mott-Schottky heterojunctions for catalysis. *Chem. Soc. Rev.* **2014**, *44*, 6593–6604. [CrossRef]
101. Chu, J.H.; Han, K.; Yu, Q.Y.; Wang, H.L.; Xi, K.; Lai, F.L.; Zhang, J.G.; Bao, Y.P. Schottky junction and multiheterostructure synergistically enhance rate performance and cycling stability. *Chem. Eng. J.* **2022**, *430*, 11. [CrossRef]
102. Cai, X.; Zeng, Z.; Liu, Y.; Li, Z.; Gu, X.; Zhao, Y.; Mao, L.; Zhang, J. Visible-light-driven water splitting by yolk-shelled $ZnIn_2S_4$-based heterostructure without noble-metal co-catalyst and sacrificial agent. *Appl. Catal. B Environ.* **2021**, *297*, 120391. [CrossRef]
103. Liu, X.; Zhang, J.; Xu, J.; Li, Y.; Du, Y.; Jiang, Y.; Lin, K. Hydroxyl-modified $Nb_4C_3T(x)$ MXene@$ZnIn_2S_4$ sandwich structure for photocatalytic overall water splitting. *J. Colloid Interface Sci.* **2023**, *633*, 992–1001. [CrossRef]

104. An, H.; Lv, Z.; Zhang, K.; Deng, C.; Yin, Z. Plasmonic coupling enhancement of core-shell Au@Pt assemblies on $ZnIn_2S_4$ nanosheets towards photocatalytic H_2 production. *Appl. Surf. Sci.* **2020**, *536*, 147934. [CrossRef]
105. Shi, Y.; Li, L.; Xu, Z.; Qin, X.; Cai, Y.; Zhang, W.; Shi, W.; Du, X.; Guo, F. Coupled internal electric field with hydrogen release kinetics for promoted photocatalytic hydrogen production through employing carbon coated transition metal as co-catalyst. *J. Colloid Interface Sci.* **2023**, *630*, 274–285. [CrossRef]
106. Sun, S.; Zhang, X.; Liu, X.; Pan, L.; Zhang, X.; Zou, J. Design and Construction of Cocatalysts for Photocatalytic Water Splitting. *Acta Phys.-Chim. Sin.* **2020**, *36*, 1905007–1905000. [CrossRef]
107. Li, H.; Xiao, J.; Vequizo, J.J.M.; Hisatomi, T.; Nakabayashi, M.; Pan, Z.; Shibata, N.; Yamakata, A.; Takata, T.; Domen, K. One-Step Excitation Overall Water Splitting over a Modified Mg-Doped $BaTaO_2N$ Photocatalyst. *ACS Catal.* **2022**, *12*, 10179–10185. [CrossRef]
108. Ma, B.; Dang, Y.; Li, D.; Wang, X.; Lin, K.; Wang, W.; Zhou, X.; Chen, Y.; Xie, T.; Zhang, X. A Yin-Yang hybrid co-catalyst (CoO_x-Mo_2N) for photocatalytic overall water splitting. *Appl. Catal. B Environ.* **2021**, *298*, 120491. [CrossRef]
109. Jing, H.; Li, H.; Yue, J.; Fan, S.; Yao, B.; Liu, S.; Fang, Z.; Wu, R.; Yang, L.; Wei, S. Synergistic effects of the Rh-S bond and spatially separated dual cocatalysts on photocatalytic overall water splitting activity of $ZnIn_2S_4$ nanosheets under visible light irradiation. *Dalton Trans.* **2023**, *52*, 2924–2927. [CrossRef]